JGR Oceans

RESEARCH ARTICLE
10.1029/2021JC017610

Ocean and Sea Ice Retrievals From an End-To-End Simulation of the Copernicus Imaging Microwave Radiometer (CIMR) 1.4–36.5 GHz Measurements

Carlos Jiménez[1,2], Joseph Tenerelli[3], Catherine Prigent[2,1], Lise Kilic[2], Thomas Lavergne[4], Sotirios Skarpalezos[5], Jacob L. Høyer[5], Nicolas Reul[6], and Craig Donlon[7]

[1]Estellus, Paris, France, [2]Observatoire de Paris, Université PSL, Sorbonne Université, CNRS, Paris, France, [3]OceanDataLab, Brest, France, [4]Research and Development Department, Norwegian Meteorological Institute, Oslo, Norway, [5]Danish Meteorological Institute, Copenhagen, Denmark, [6]Laboratoire d'Océanographie Physique et Spatiale, Univ. Brest, Ifremer, CNRS, Brest, France, [7]European Space Agency (ESA), Noordwijk, The Netherlands

Abstract The Copernicus Imaging Microwave Radiometer (CIMR) is currently being implemented by the European Space Agency (ESA) as a Copernicus Expansion Mission primarily designed to observe the Polar Regions in support of the Integrated European Policy for the Arctic. It is a conically scanning microwave radiometer with polarized channels centered at 1.414, 6.925, 10.65, 18.7, and 36.5 GHz and channel NEΔT between 0.2 and 0.7 K. A large rotating deployable mesh reflector will provide real-aperture resolutions ranging from <60 (1.4 GHz) to <5 km (36.5 GHz). To evaluate CIMR retrieval performance, a simplified end-to-end simulation of the mission has been carried out. The simulation includes important processes and input parameters, such as test geophysical datasets, forward models, an instrument simulator, and retrieval algorithms to derive the key mission geophysical products. The forward modeling is tested by producing Brightness Temperatures (TBs) from 4 global scenes. A comparison with current observations of the open ocean and sea ice at similar frequencies confirmed the realism of the simulations. The produced top-of-atmosphere TBs are converted to Antenna brightness Temperatures (TAs), taking into account the instrument design, and are then inverted to retrieve Sea Ice Concentration (SIC), Sea Surface Temperature (SST), and Sea Surface Salinity (SSS). Evaluating the retrieval performance showed that the simulated CIMR instrument can provide SST, SSS, and SIC measurements with precisions and spatial resolutions conforming with the mission requirements. The evaluation also highlighted the challenges of observing the Arctic environment and put in perspective CIMR capabilities compared with current instruments.

Plain Language Summary The Copernicus Imaging Microwave Radiometer (CIMR) satellite instrument is currently being implemented to observe the Polar Regions. It will measure different variables, including the temperature and salinity of the ocean surface, and the sea ice extension in the polar ice caps. To help design the instrument, the first instrument concept has been computer simulated. Together with simulations of the radiation emitted by the oceans, it allows reproducing what the instrument antennas will measure. This is followed by further computations that apply mathematical algorithms to the simulated measurements to estimate the values of the ocean and ice parameters of interest. Studying these simulated measurements is then used to see whether the CIMR instrument concept is suitable to achieve the mission goals, and how much better CIMR will measure compared with existing instruments already observing similar variables. Although more work is required to keep refining the instrument and its computer simulations, this study shows that CIMR can achieve its mission goals, measuring more accurately and with better spatial resolution than previous instruments, and greatly contributing to monitoring the rapid changes expected to take place in the Polar regions in the years to come.

Key Points:

- A new passive microwave satellite instrument measuring simultaneously between 1.4 and 36.5 GHz is under development
- A first simplified end-to-end simulation of the instrument focusing on the inversion of the simulated radiances is presented
- Sea surface temperature and ice concentration are retrieved with better precision and spatial resolution than current microwave instruments

Correspondence to:
C. Jiménez,
carlos.jimenez@estellus.fr

Citation:
Jiménez, C., Tenerelli, J., Prigent, C., Kilic, L., Lavergne, T., Skarpalezos, S., et al. (2021). Ocean and sea ice retrievals from an end-to-end simulation of the Copernicus Imaging Microwave Radiometer (CIMR) 1.4–36.5 GHz measurements. *Journal of Geophysical Research: Oceans*, *126*, e2021JC017610. https://doi.org/10.1029/2021JC017610

Received 25 MAY 2021
Accepted 9 NOV 2021

1. Introduction

The Copernicus Imaging Microwave Radiometer (CIMR) is a satellite system developed as part of the European Union Copernicus program expansion activities. CIMR is designed to monitor the rapid Earth system changes taking place in the Arctic in response to the Integrated European Policy for the Arctic. Prioritized user needs to be expressed by the European Commission Polar Expert Group (Duchossois, Strobl, Toumazou, Antunes, Bartsch, Diehl, & Nordbeck, 2018; Duchossois, Strobl, Toumazou, Antunes, Bartsch, Diehl, & de Witte, 2018)

are the foundation of the CIMR mission that is fully described in the Mission Requirements Document (Donlon, 2020). The aim of the mission is to provide high-spatial resolution microwave imaging radiometry measurements and derived products with global coverage and sub-daily revisit in the polar regions and adjacent seas to address Copernicus user needs. Its main challenges are (1) to provide high spatial resolution 5 km Ka/Ku band measurements of sea ice parameters that provide an enhanced capability compared to 89 GHz solutions that are challenged by atmospheric effects; (2) to provide high spatial resolution (15 km) C/X band measurements of global coverage sea surface temperature with quasi all-weather capability and rapid (1–2 days) revisit, and; (3) to maintain an L-band measurement capability to continue the legacy of sea surface salinity and soil moisture parameters from previous L-band missions.

At the heart of the CIMR mission design is the need to measure fundamental quantities associated with large-scale ocean-cryosphere-atmosphere processes in the Arctic. Sea ice is part of the oceanographic "system" and the physics of eutectoid changes and the thermodynamically driven state of seawater is at the heart of the system. Level-2 products include Sea Ice Concentration (SIC), Sea Surface Temperature (SST), Sea Surface Salinity (SSS), Sea Ice Drift (SID), Sea Ice Thickness (SIT), Snow Depth on sea ice (SND), and Sea Ice Surface Temperature (SIST). As part of the mission design, which includes contiguous global coverage, CIMR will also have the capability to deliver a variety of additional parameters including ice-type, terrestrial snow extent, ice surface temperature, wind speed over the ocean, soil moisture, and vegetation indices. Data products are to be operationally available within 3 hr of sensing at the user point of pickup, with a capability to provide specific products within 1 hr of sensing in support of Arctic navigation safety.

The CIMR instrument concept is based around a conically scanning multi-frequency microwave radiometer with a 55° incidence angle with the Earth surface. Its design partly inherits from previous studies conducted at ESA for the Multifrequency Imaging Microwave Radiometer (MIMR) (Bernard et al., 1990). CIMR measurements will be made using a forward scan arc followed ∼260 s later by a second measurement of the same location using a backward scan arc. Channels in bands L, C, X, Ku, and Ka, centered at 1.414, 6.925, 10.65, 18.7, and 36.5 GHz, respectively, are included in the mission design. The measurements will be acquired in vertical (V) and horizontal (H) polarizations, with on board the spacecraft and on ground strategies put in place to mitigate Radio Frequency Interference (RFI) contamination. Modified Stokes parameters will be computed on-board the spacecraft. The spatial resolution of the real-aperture antenna for the C/X-band channel is at least 15 km, and 5 and 4 km, and for the Ku and Ka-band channels, respectively. The L-band channel will have a real-aperture resolution of at least 60 km, fundamentally limited by the size of the reflector and the focus of the L-band feed. However, all channels will be oversampled along and across-track by 20% allowing gridded products to be generated at better spatial resolutions. Channel Noise Equivalent Delta Temperature (NEΔT) is 0.2–0.7 K with total standard uncertainty at processing level L1B (instrument data processed to sensor units) better than 0.5 K (L,C,X), 0.6 K (Ku), and 0.7 K (Ka).

CIMR will be flying in a dawn-dusk orbit deploying a wide-swath (>1,900 km), which will result in a 95% global coverage every day, better than daily coverage poleward of 55°N and 55°S, and no gap in coverage at the poles themselves. It is expected to operate in synergy with the European Organisation for the Exploitation of Meteorological Satellites (EUMETSAT) MetOp-SG(B) mission so that collocated and contemporaneous measurements between CIMR and MetOp-SG(B) Microwave Imaging Radiometer (MWI), Ice Cloud Imager (ICI), and Scatterometer (SCA) measurements can be made available within ±10 min in the polar regions.

An information content analysis was carried out by Kilic et al. (2018) to illustrate the expected retrieval performance of CIMR. This analysis is extended here by performing actual retrievals from an end-to-end simulation of the CIMR observations. Being this a first simulation of the CIMR observations carried out during the mission Phase A/B1 (Mission Feasibility/Preliminary Definition), the work focuses on realistically simulating the vertically and horizontally polarized brightness temperatures to be observed by a preliminary configuration of the instrument, together with inverting the main mission retrieval parameters from the simulated measurements to showcase the expected CIMR performance in the context of the existing current instruments. For the latter, this study concentrates on evaluating the retrieval performance of SIC and SST. Measuring SIC and SST are the two first mission objectives, and therefore critical to deriving the mission requirements (Donlon, 2020). The impact of the CIMR channel selection for SST retrievals is discussed in Nielsen-Englyst et al. (2021), and sensitivity analysis of CIMR observations over the Arctic Ocean is presented in Kilic et al. (2021). The third main objective is to assure continuity of L-band, and, to illustrate the value of having the 1.4 GHz channel on board, the

Table 1
Summary of the Requirements on the Sea Ice Concentration, Sea Surface Temperature, and Sea Surface Salinity Measurements for the Copernicus Imaging Microwave Radiometer Mission, in Terms of Spatial Resolution, Uncertainty, and Temporal Sampling (Donlon, 2020)

Variable	Spatial resolution	Uncertainty[a]	Temporal sampling
Sea Ice Concentration (SIC)	5 km	<5%	Sub-daily
Sea Surface Temperature (SST)	15 km	<0.3 K	Sub-daily
Sea Surface Salinity (SSS)	5 km	<0.3 pss[b]	Monthly

[a]The value for SST is calculated for a theoretical retrieval as the mode value of daily global ocean average discrepancies assuming no uncertainty in the validation dataset, while for SIC and SSS it is a standard retrieval uncertainty. [b]Practical Salinity Scale 1978 (PSS-78) are used, following UNESCO guidelines (UNESCO, 1985). Although salinity measured using PSS-78 does not have units, the suffix "pss" is sometimes used in the text and figures to distinguish the values of salinity, rates, and variance.

Sea Surface Salinity (SSS) retrieval performance is also studied. The main mission requirements for the measurements of SIC, SST, and SSS are summarized in Table 1. Analyses of the retrieval performance of other mission variables are left for further studies. A full list of the variables can be found in Donlon (2020).

The study is organized as follows. Section 2 describes the simulating tools and datasets used to perform the inversion, including reference geophysical scenes, the forward radiative transfer modeling, an instrument simulator, and retrieval schemes. The specific configuration of the preliminary CIMR concept adopted for the study is also detailed in this section. Examples of simulated observations are analyzed in Section 3.1 and compared with radiometer observations from currently operated similar types of satellite missions. Section 3.2 discusses the retrievals of the selected geophysical products derived from the simulated CIMR observations. Finally, Section 4 concludes the study.

2. Methods and Datasets

An overview of the framework used to simulate the CIMR inversions and evaluate the derived retrieved products is presented in Figure 1. First, global geophysical fields are collected. They include all the relevant surface and atmospheric information necessary to feed a radiative transfer model. The forward model accounts for the interaction of the microwave radiation with the surface and atmospheric components, under the instrument observing conditions (e.g., frequency, incidence angle), and simulates top-of-atmosphere brightness temperatures (TBs). The instrument simulator convolves the antenna patterns of each channel feed horn with the modeled TBs and adds the corresponding instrument noise to produce the antenna TBs (TAs). The retrieval algorithms are applied to the simulated TAs, to estimate the selected geophysical variables that would be derived from CIMR. The resulting geophysical parameters are then

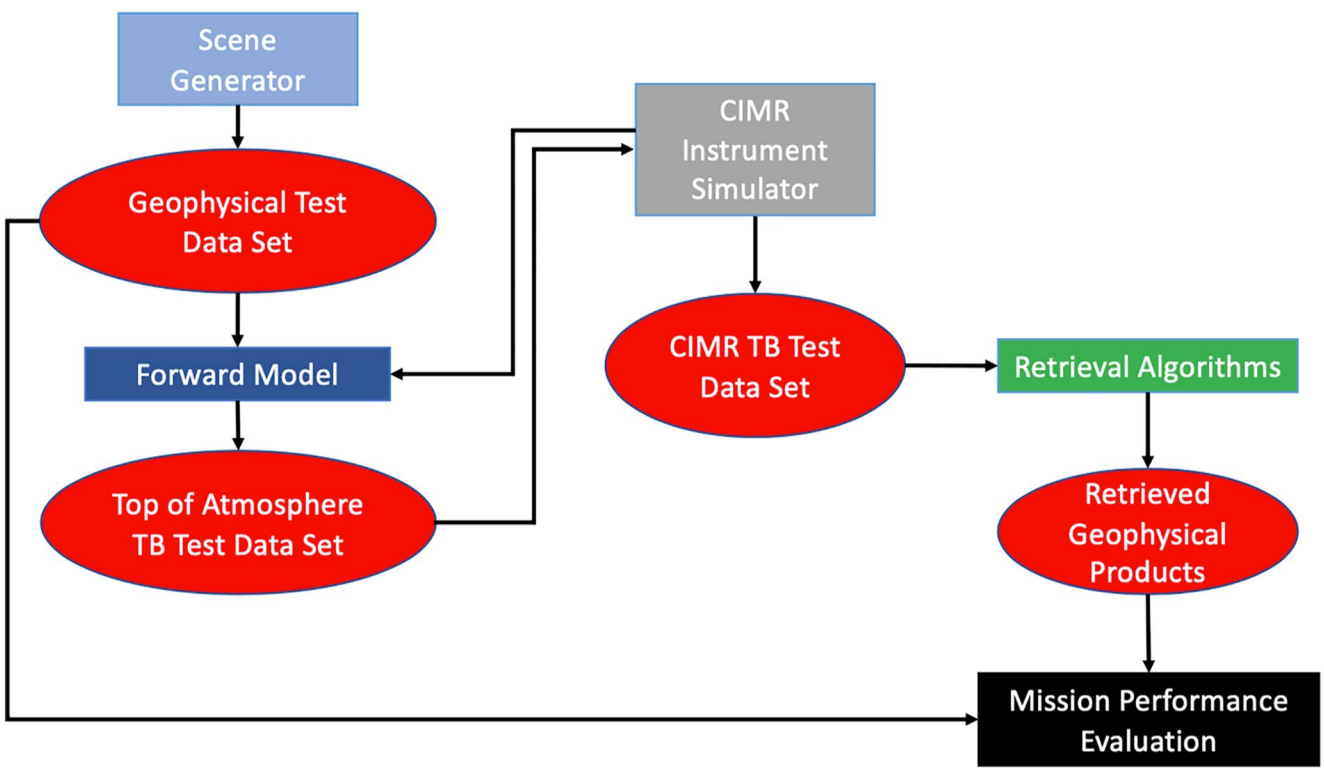

Figure 1. Schematic overview of the framework used to simulate the Copernicus Imaging Microwave Radiometer observations.

Table 2
Summary of the Main Inputs Included in the Geophysical Test Datasets

Variable	Source
ATMOSPHERE	
Temperature Profile	ERA5[a]
Water Vapor Profile	ERA5
Liquid Water Profile	ERA5
Total Column Water Vapor	ERA5
Total Column Liquid Water	ERA5
Near Surface (2m) Air Temperature	ERA5
Near Suface (2m) Dew Point	ERA5
OCEAN	
Sea Surface Temperature	MEaSUREs MUR[b]
Sea Surface Salinit	CMEMS[c]
Ocean Wind Speed	RSS CCMP[d]
Mean Sea Level Pressure	ERA5
SEA ICE	
Sea Ice Concentration	ASI[e]
Sea Ice Thickness	CMEMS
Sea Ice Type	C3S CDR[f]
Sea Ice Surface Temperature	ERA5
Sea Ice Surface Pressure	ERA5
LAND	
Surface Skin Temperature	ERA5
Land Surface Pressure	ERA5

Note. Four global scenes corresponding to dates 2016/12/17, 2017/03/14, 2017/06/15, and 2017/09/15 are used in this study. The original resolution of ERA5 products is 31 km, Sea Surface Temperature 1 km, the Sea Surface Salinity and Sea Ice Thickness 8 km, Ocean Wind Speed 25 km, Sea Ice Concentration 5 km, and Sea Ice Type 50 km.

[a]European Center for Medium-Range Weather Forecasts (ECMWF) ERA5 reanalysis. [b]Sea Surface Temperature Making Earth System Data Records for Use in Research Environments (MEaSUREs) Multi-scale Ultra-high Resolution (MUR). [c]Copernicus Marine Environment Monitoring Service (CMEMS) Global Analysis (GA). [d]Remote Sensing Systems (RSS) Cross-Calibrated Multi-Platform (CCMP) Analysis. [e]University of Bremen ARTIST Sea Ice (ASI) [f]Copernicus Climate Change Services (C3S) Climate Data Record (CDR).

compared to the initial surface and atmospheric fields, to evaluate the CIMR performance.

2.1. The Geophysical and Observation Test Data Set

Four geophysical global scenes, corresponding to the dates 2016/12/17, 2017/03/14, 2017/06/15, and 2017/09/15, that is, one day per season, are selected. The geophysical fields include all the necessary variables required to run the forward model, for the surface as well as the atmosphere. Table 2 summarizes the main variables. Most information comes from the European Center for Medium-Range Weather Forecasts (ECMWF) ERA5 reanalysis with a grid resolution of 31 km (Hersbach et al., 2020), completed with other sources for the open ocean and sea ice. In addition to the geophysical fields, coincident Soil Moisture Active Passive (SMAP) (Chaubell et al., 2019) and Advanced Microwave Scanning Radiometer 2 (AMSR2) (Maeda et al., 2016) observations are stored, for a preliminary assessment of the forward model and retrieval products. Similar to CIMR, SMAP, and AMSR2 have real aperture antennas, measuring the vertically and horizontally polarized radiation at the frequencies to be observed by CIMR. The instrument's main characteristics are given in Table 3.

All fields have been harmonized from their native resolution to a common 4 km grid using bi-linear interpolation (ocean and atmospheric products) and nearest neighbor interpolation (sea ice products and observations), followed by post-processing to mitigate some obvious data inconsistencies related to using products from different sources, such as sea-surface cells having assigned a sea-ice temperature or a coastal land surface temperature. Other inconsistencies produced by the harmonization process can still remain. Nevertheless, the impact on the overall statistics of the simulations is assumed small given the large number of cases simulated, and we judge the set of scenes realistic enough to simulate the CIMR observations.

2.2. The Forward Model

The TBs are calculated with a radiative transfer equation that accounts for: (a) the contribution from the surface itself, attenuated by the atmosphere, (b) the downwelling atmospheric signal, reflected by the surface, and attenuated by the atmosphere, and (c) the direct upwelling signal from the atmosphere. In the processing, a common forward model is used across all frequencies, from 1.4 to 36 GHz. The produced TBs are the top-of-atmosphere TBs for all channels except the L-band. Data in this frequency band are indeed impacted by the ionosphere, through Faraday rotation, and the L-band TBs are therefore estimated at the top of the ionosphere. TBs will then be used as input to the instrument simulator to produce the antenna TAs, that is, the TBs observed by the CIMR radiometers. The contribution of Earth-surface reflected extra-terrestrial (Sun, celestial sky) signals to the top-of-atmosphere TBs is significant for the lowest frequencies of CIMR, and it also needs to be accounted for in the radiative transfer modeling.

2.2.1. Atmospheric Transmission Model

The atmospheric contribution is calculated with the Rosenkranz model (Rosenkranz, 2017; https://doi.org/10.21982/M81013). It includes the latest improvements in atmospheric gas absorption as well as a formulation for the non-scattering contribution of the liquid water particles.

Table 3
Soil Moisture Active Passive and Advanced Microwave Scanning Radiometer 2 Main Instrumental Characteristics (Channels Shared With Copernicus Imaging Microwave Radiometer)

Frequency	Band	Spatial resolution[a]	Incidence angle	NEΔT
SMAP				
1.4 GHz	L	37 × 47 km	40°	0.9 K
AMSR2				
6.925 GHz	C	35 × 62 km	55°	0.3 K
10.65 GHz	X	24 × 42 km	55°	0.6 K
18.7 GHz	Ku	14 × 22 km	55°	0.6 K
36.5 GHz	Ka	7 × 12 km	55°	0.6 K

[a]Spatial resolution corresponds to the instantaneous -3db beamwidth footprint size.

2.2.2. Sea Surface Emissivity Model

The ocean emissivity varies primarily with SST, SSS, and the Ocean Wind Speed (OWS). It also depends upon the observation parameters, such as frequency, incidence angle, and polarization. Recently, ocean radiative transfer models have been systematically compared to existing satellite observations, at 1.4 GHz using SMAP, and between 6 and 89 GHz using AMSR2 (Kilic et al., 2019). At this stage, the Remote Sensing Systems (RSS) empirical model (Meissner & Wentz, 2012; Meissner et al., 2014) is selected, as it covers all CIMR observing bands and best matches satellite observations, with less discrepancies as a function of SST and OWS. This model is partially fitted to satellite observations, with the Special Sensor Microwave/Imager (SSM/I) and WindSat observations between 6-89 GHz (Meissner & Wentz, 2012), and with Aquarius observations at 1.4 GHz (Meissner et al., 2014). It can be used to model the four modified Stokes parameters to be measured by CIMR, but only the vertically and horizontally polarized TBs are considered here. The third and fourth Stokes parameters will be useful to support the CIMR retrievals (e.g., Faraday rotation correction, wind vector measurements), but they are not used in the retrievals presented here, so only the vertical and horizontal components are computed in these first simulations. Notice that a simple bias correction is implemented using the global comparison of the RSS model with observations of Kilic et al. (2019) by a lookup table providing the bias to be subtracted as a function of SST and OWS conditions.

2.2.3. Sea Ice Emissivity Parameterization

Sea ice is a very complex medium and physically-based emissivity models are still challenging to apply for large scale simulations, at multiple frequencies and polarizations (Burgard et al., 2020; Tonboe, 2010). Sea ice emissivities from observations can be derived if the required coincident information can be made available (Mathew et al., 2009). Here we explore this alternative by first deriving sea ice emissivities from the ESA Sea Ice Climate Change Initiative project Round Robin Data Package (RRDP) (Pedersen et al., 2019), followed by developing an observation-based parameterization using the previous emissivity estimates. The RRDP contains TBs over 100% sea ice from the Soil Moisture and Ocean Salinity (SMOS) (Kerr et al., 2001) and AMSR2 instruments. SMOS synthetic aperture antenna measures at 1.4 GHz with incident angles from nadir to 65°, while the AMSR2 radiometer observed at CIMR 55° incident angle. The TBs are provided together with collocated relevant geophysical information.

Here the RRDP is used to provide a realistic sea ice emissivity, using the coincident SMOS and AMSR2 TBs at the CIMR incident angle, with the atmospheric contribution and the surface temperature modulation previously subtracted using the ancillary information also contained in the RRDP. Once the sea ice emissivity is produced for all cases in the RRDP at a given frequency and polarization, the emissivities are binned as a function of the 2-meter air temperature, the ice age (first year or multi-year), and the snow depth. The air temperature and ice age are given in the RRDP, while the snow depth is estimated from the AMSR observations using the parameterization derived in Kilic et al. (2019). The results are stored in a lookup table, for Arctic and Antarctic regions separately.

2.2.4. Land Surface Emissivity Parameterization

The physical modeling of the microwave land surface emissivity is also challenging. The alternative is to directly calculate the emissivities from microwave satellite observations, removing the atmospheric contribution and the modulation by the land surface temperature. Their frequency, angular, and polarization dependencies have been studied and the Tool to Estimate Land Surface Emissivity at Microwaves and Millimeter Waves (TELSEM2; Wang et al., 2017) has been derived from these works. This parameterization provides estimates of the microwave land surface emissivity, as a function of frequency, incidence angle, polarization, location, and month in the year, along with an error estimation, and is adopted for the forward model implemented here.

Table 4
Summary of the Copernicus Imaging Microwave Radiometer Orbit and Preliminary Instrument Design Simulated in This Study

Orbit altitude (km)					800
Reflector rotation (rpm)					6.5
Ground Swath (km)					1,900
Incident Angle (deg)					55
Polarization					V H
Channel frequency (GHz)	1.4	6.9	10.6	18.7	36.5
Number of horns	1	5	5	10	10
Integration time (ms)	70.8	14.7	13.3	6.5	4.2
Bandwidth (MHz)	26	650	100	200	1,000
Footprint size[a] (km)	36 × 64	11 × 19	7 × 13	4 × 6	3 × 5
NEΔT (K)	0.3	0.2	0.3	0.3	0.7

[a]Footprint size given here corresponds to the minor and major axis of the ellipse defining the -3db beamwidth instantaneous field of view.

2.3. The Instrument Simulator

The instrument simulator models the operations needed to calculate TAs, equivalent to the measurements CIMR will make, from the TBs. For the practical implementation, a specific orbit geometry, instrument design, and a set of antenna patterns spatially extended to largely cover the main lobe are adopted here. Their main characteristics are given in Table 4. This configuration is used here for a first evaluation of the CIMR performance during Phase A/B1 of the mission development.

The derivation of TAs starts with a calculation of the orbit and viewing geometry in order to find the Earth target locations. This is done by applying a series of geometrical transformations between the antenna and different geographical frames. Then a series of new transformation matrices to transport the Stokes vector between the Earth target and the antenna polarization basis are calculated. These transformation matrices, together with discretized antenna patterns, permit the numerical calculation of the TAs. The full derivation of the instrument simulation, together with the antenna simulated patterns can be found in Tenerelli (2019). Note that due to the instrument rotation rate and the satellite velocity, the antenna patterns move during the integration times, and the antenna pattern calculation needs to take into account the integration time of the receiver. This is mainly noticeable at L-band given the large integration times used to provide the L1B measurements. The smearing of the antenna footprints is then accounted for in the simulator, and the TAs are consequently derived with the antenna effective fields of view.

For L-band, additional processing is required, including the calculation of the Faraday rotation angle, estimation of the Sun and Galactic glint contributions for the given viewing geometry, and calculation of main beam TBs below the ionosphere. The Sun and Galactic glint components are calculated following methodologies developed by (Reul et al., 2007, 2008; Tenerelli et al., 2008). For that purpose, an L-band sky map is generated, including the hydrogen HI line, the L-band continuum, and the cosmic background.

2.4. The Ice-Free Ocean Retrieval Algorithm

To fully benefit from the CIMR multi-frequency measurement combination, the proposed inversion methodology is based on an optimal estimation algorithm (Rodgers, 1976, 2000). This inversion scheme allows to optimally combine the information from the simultaneous observations at all CIMR frequencies with the existing *a priori* knowledge about the retrieval variables of interest, providing a consistent dataset of jointly retrieved geophysical variables. Given the large number of variables that can be potentially retrieved from CIMR (see Donlon, 2020), this is also useful to provide a common starting point for more specialized retrievals that can further refine these first estimates, or retrieve new parameters, mitigating the problem of potential internal consistency when *a priori* knowledge is sourced from external datasets.

In this approach, the retrieval can be estimated using an iterative procedure to solve the implicit equation:

$$x = x_a + S_a \cdot K_x^T \cdot S_\epsilon^{-1} \cdot (y - F(x)) \quad (1)$$

where x is the state vector containing the geophysical variables to be retrieved, x_a is the *a priory* value of x, S_a is the *a priori* uncertainty covariance matrix, y is the measurement vector containing the TBs to be inverted, $F(x)$ the radiative transfer forward model evaluated at x, K_x the Jacobians of F (i.e., the derivative of F with respect x), and S_ϵ is the covariance matrix of the measurement noise. The equation is solved by a Marquardt-Levenberg iterative scheme (Marks & Rodgers, 1993). A step of the iteration is given by:

$$x_{i+1} = x_i + (K_{x_i}^T \cdot S_\epsilon^{-1} \cdot K_{x_i} + S_\epsilon^{-1} + \gamma \cdot I)^{-1} \cdot [K_{x_i}^T \cdot S_\epsilon \cdot (y - F(x_a)) + S_a^{-1} \cdot (x_a - x_i)] \quad (2)$$

where x_i is the solution after iteration i, I is the identity matrix, and γ is a parameter controlling the trade-off between steepest-descent and Newtonian iteration (see Marks & Rodgers, 1993 for more details). The iteration procedure is initiated with $x_1 = x_a$, and stopped after a number of iterations once satisfactory convergence is reached. The corresponding error covariance matrix for each solution x can be calculated as:

$$S = (K_x^T \cdot S_\epsilon^{-1} \cdot K_x + S_a^{-1})^{-1} \quad (3)$$

allowing to give an estimation of the retrieval error for each retrieved state.

The Jacobians K_x for different ocean and atmospheric observing scenarios were studied in Kilic et al. (2018), together with an analysis of the theoretical retrieval error derived by computing Equation 3 for different instrument conditions. As the TBs observed at the CIMR frequencies showed sensitivity to the ocean variables SST, SSS, and OWS, and the atmospheric variables Total Column Water Vapor (TCWV) and the Total Column Liquid Water (TCLW), the retrieval state vector x includes all these variables to allow the inversion algorithm to exploit all information contained in the TBs. Only the retrieval performance of SST and SSS is evaluated here, but the retrieved state of the remaining variables can equally be used to provide an updated estimate, consistent with the observed TBs.

The *a priori* information, that is, our *a priori* knowledge about the state vector x, is needed for the ocean parameters as well as for the atmosphere, close in time and space to the measured TAs. For these simulations, the *a priori* information comes from the ERA5 fields, with the associated uncertainty derived by inspecting the global variability of its daily fields, as in Kilic et al. (2018). The same standard deviation values are adopted here to populate S_a: 3.3 K for the SST, 1.3 m/s for OWS, and 1 psu for the SSS. For TCWV and TCLW, a relative uncertainty of 20% for TCWV and 100% for TCLW is applied, so the *a priori* uncertainty is state dependent and changes for each atmospheric situation. Notice that the off-diagonal elements of S_a are set to zero. In further simulations the existing inter-correlations in the state vector x could be studied and incorporated to S_a, which should help to better characterize the inversion problem.

An estimate for x_a is also needed as a starting point of the iterative inversion. Here, the TBs of the y vector to be inverted are produced with the geophysical fields presented in Section 2.1, so those fields cannot be used to populate x_a. However, they can be modified by randomly perturbing the original values for each simulation with the uncertainty given by S_a, and using the modified values to fill x_a. This procedure assures that for each simulated y to be inverted, the corresponding x, x_a, and S_a are consistent with the statistical retrieval assumptions.

The covariance matrix of the instrumental noise (S_ϵ) is assumed diagonal, and populated with the NEΔT of each channel. The concrete values are taken from Table 4 when inverting CIMR simulated TBs, or from Table 3, when inverting SMAP and AMSR2 simulated TBs. Notice that for CIMR, both fore and aft views of the instrument are expected to be used simultaneously. Although the exact intersection of the fore and aft views across tracks needs to be further quantified, for this first simulation we assume that the fore and aft views match perfectly, so the NEΔT values given in Table 4 are applied with a ratio of $1/\sqrt{2}$. Notice also that other sources of error impacting the values assumed in S_ϵ will also exist, such as forward model errors, instrument calibration errors, imperfect knowledge of the antenna patterns, residuals from the RFI mitigation strategies, incomplete removal of Faraday rotation and galactic noise, or propagation of uncertainty due to L1C resampling. They are neglected here but will require quantification in more advanced phases of the mission.

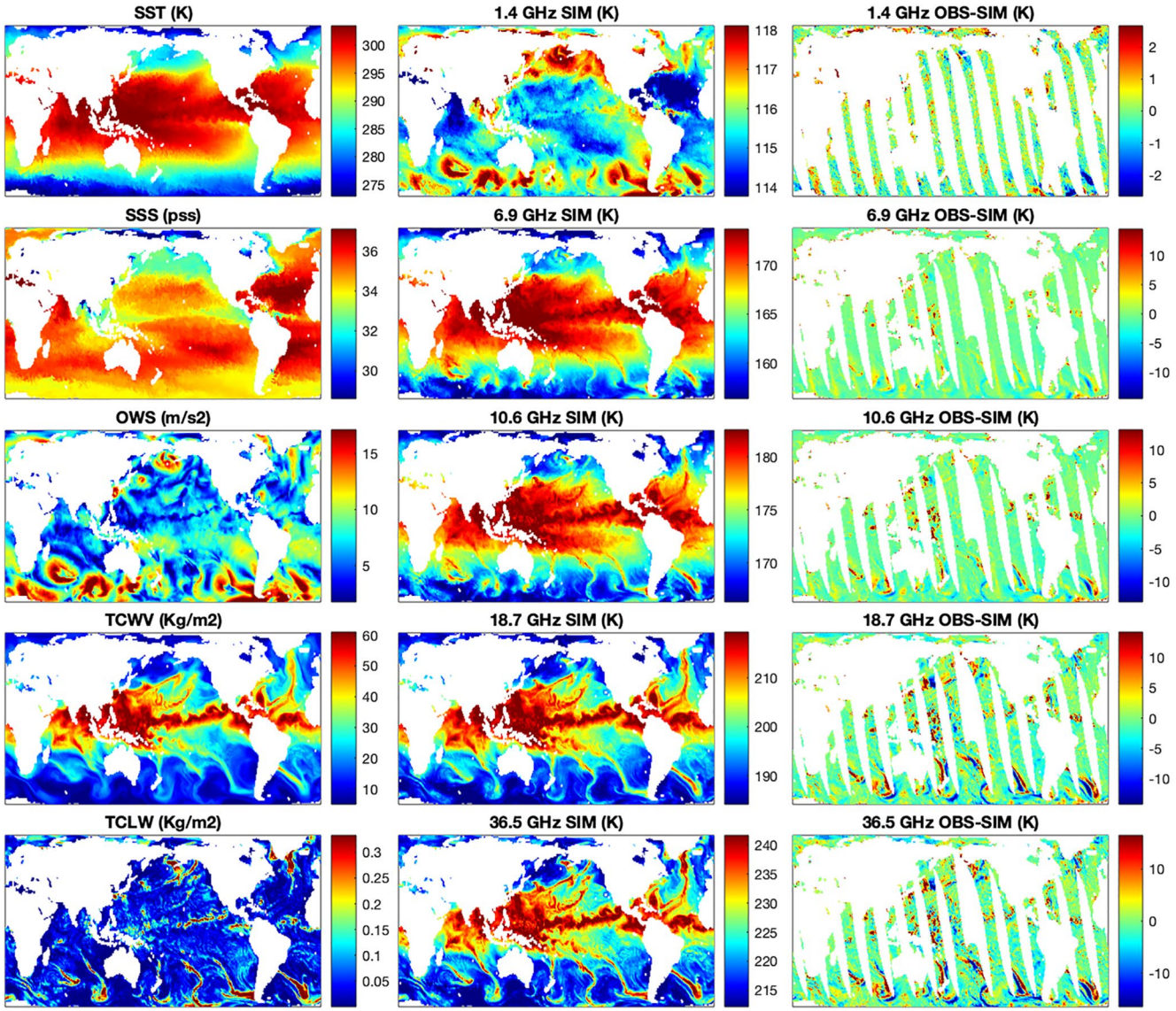

Figure 2. Open ocean radiative transfer simulations at the Copernicus Imaging Microwave Radiometer vertically polarized channels for the day 2017/09/15. Plotted the sea surface temperature, sea surface salinity, ocean wind speed, total column water vapor, and total column liquid water global fields (left), the simulated top-of-atmosphere brightness temperature (TBs) (middle), and their differences with the collocated SMAP (1.4 GHz) and AMSR2 (6.9–36.5 GHz) TBs (right).

The joint inversion of all CIMR observing channels requires postprocessing of the L1B TAs to overcome the spatial resolution differences of the CIMR channels. This can be achieved by processing of the original L1B measurements into L1C products containing synthesized TAs with fields of view matched to the location and resolution of a target frequency (e.g., Maeda et al., 2016). The corresponding procedure for CIMR TAs is still under discussion, and it has not yet been implemented in these first simulations. Instead, a simplified scheme based on averaging (finer to coarser resolutions) or sampling (coarser to finer) TAs to match footprint center positions is implemented. As the 6.9 GHz channels present the maximum sensitivity to the SST variations, and SST is the primary product for the ice-free ocean, the optimal estimation method will be applied to the TAs matched to the 6.9 GHz footprints. More elaborate schemes based on antenna pattern matching techniques will be investigated in the next mission phases.

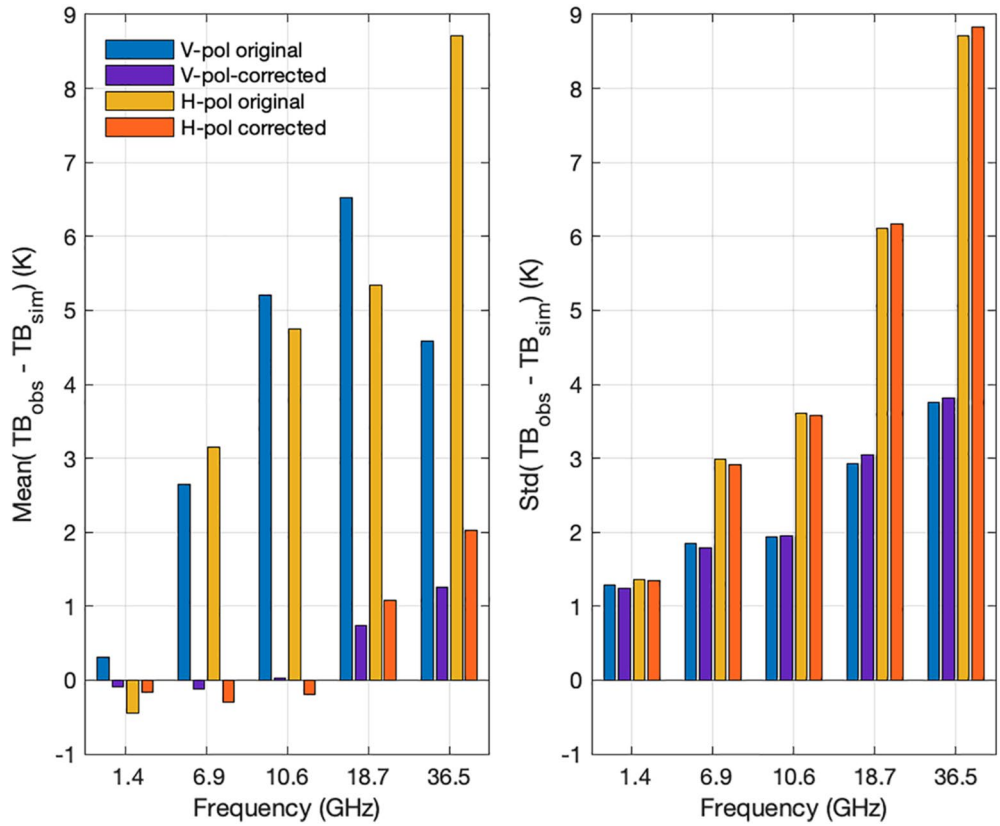

Figure 3. Statistics of the comparison of observed and simulated bright temperature (TB) for day 2017/09/15. Plotted the mean (left) and standard deviation (right) of the vertically (V-pol) and horizontally (H-pol) polarized TB difference between the observations and the simulations. The statistics are presented before (original) and after adding the bias correction implemented in the radiative transfer module (corrected).

2.5. The Sea Ice Concentration Retrieval Algorithm

The SIC retrievals are based on the strong contrast in emissivity between open water (low emissivity, low TB) and sea ice (high emissivity, high TB). The contrast depends on frequency, polarization, and the type of sea ice. The algorithm implemented here is a hybrid algorithm similar to those implemented in the Ocean and Sea Ice Satellite Application Facility (OSI SAF) and ESA Climate Change Initiative (ESA CCI) processing chains. This hybrid algorithm combines two SIC algorithms: a first one that is tuned to perform better over open-water and low-concentration conditions, producing the Best Open Water (B_{OW}) estimation, and a second one that is tuned to perform better over closed-ice and high-concentration conditions, producing the Best Closed Ice (B_{CI}) values. The final SIC is obtained by linearly combining the estimates from these two algorithms (Lavergne et al., 2019; Tonboe et al., 2016).

Both SIC estimations, the B_{OW} and B_{CI}, are based on a linear combination of TBs. In an operational application, the combination coefficients will change on a daily basis and will depend on the region investigated (Arctic and Antarctic) due to the dynamic tuning of the tie points (the observed TBs associated with the open water and closed ice conditions used to derive the coefficients) (Lavergne et al., 2019). Note also that atmospheric correction of the TBs, correction for the land surface contribution, and weather filters would also be used in the operational algorithms (Lavergne et al., 2019). Here the algorithm is simplified by just using a particular set of coefficients derived using the TBs and corresponding SIC values compiled in the RRDP, without any TB corrections. The Best Open Water B_{OW} and B_{CI} SIC estimations are implemented by:

$$B_{OW} = 2.40 \cdot 10^{-2} \cdot TB_{19V} - 3.61 \cdot 10^{-3} \cdot \cdot TB_{37H} - 8.59 \cdot 10^{-3} \cdot TB_{37V} - 2.17 \quad (4)$$

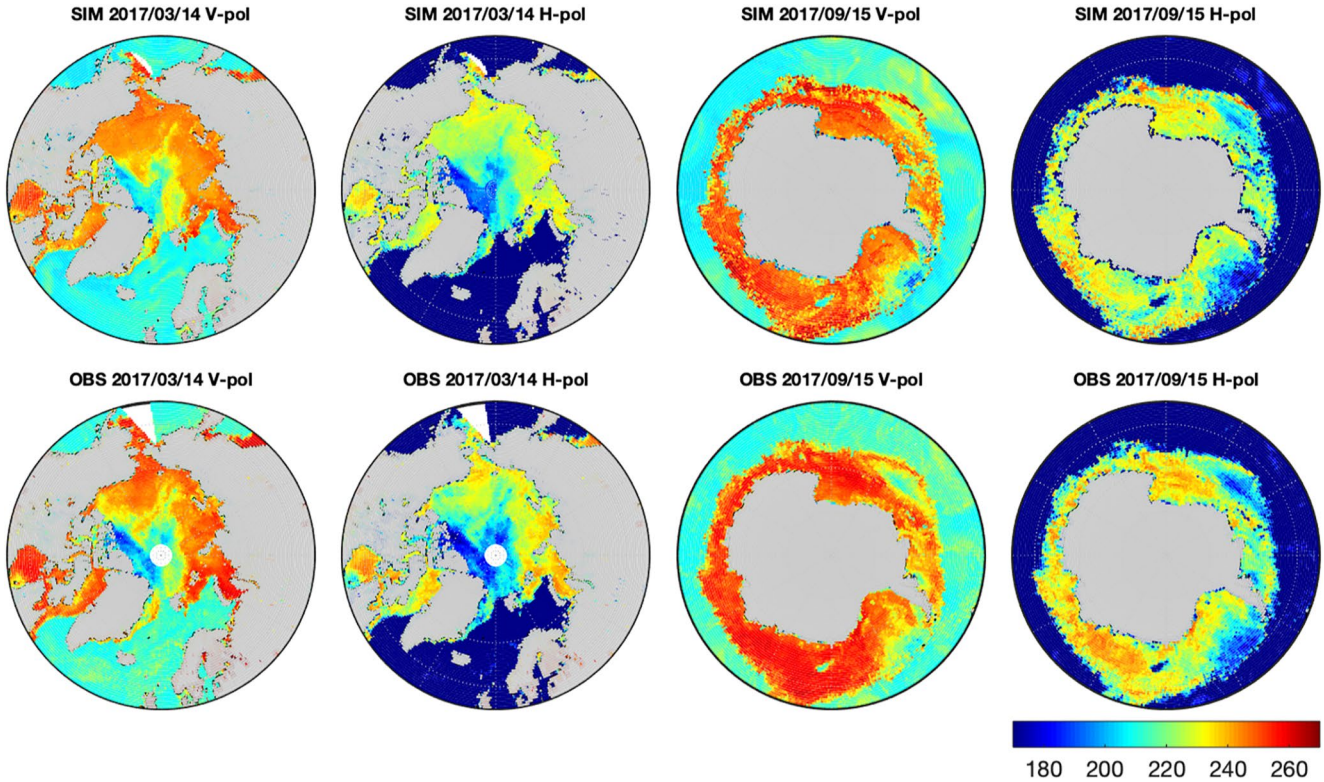

Figure 4. Sea ice radiative transfer simulations at the Copernicus Imaging Microwave Radiometer 18.7 GHz vertically (V-pol) and horizontally (H-pol) polarized channels for the days 2017/3/14 and 2017/09/15. Plotted the Arctic (left) and Antarctic (right) simulated (SIM, top) and the observed Advanced Microwave Scanning Radiometer 2 (OBS, bottom) brightness temperatures in K.

$$B_{CI} = 1.48 \cdot 10^{-2} \cdot TB_{19V} - 5.79 \cdot 10^{-3} \cdot \cdot TB_{37H} - 1.34 \cdot 10^{-3} \cdot TB_{37V} - 8.14 \cdot 10^{-1} \tag{5}$$

where TB_{19V} and TB_{37V} are, respectively, the vertically polarized TBs at 19 and 37 GHz, and TB_{37H} the horizontally polarized TB at 37 GHz. The final SIC estimate is given by

$$SIC = w_{OW} \cdot B_{OW} + (1 - w_{OW}) \cdot B_{CI} \tag{6}$$

where the weight w_{OW} is defined as

$$w_{OW} = \begin{cases} 1 & \texttt{if} \quad B_{OW} < 0.7 \\ 0 & \texttt{if} \quad B_{OW} > 0.9 \\ \dfrac{B_{OW} - 0.7}{0.2} & \texttt{if} \quad B_{OW} \in [0.7 - 0.9] \end{cases} \tag{7}$$

The algorithms uncertainty results mainly from the variability of the open water and ice tie-points used to derive Equations 4 and 5 coefficients. It can be estimated as a quadratic function of SIC by the expressions:

$$\sigma^2_{OW} = (1 \quad - B_{OW})^2 \cdot \sigma^2_{OW_W} + B^2_{OW} \cdot \sigma^2_{OW_I} \tag{8}$$

$$\sigma^2_{CI} = (1 \quad - B_{CI})^2 \cdot \sigma^2_{CI_W} + B^2_{CI} \cdot \sigma^2_{OW_I} \tag{9}$$

where $\sigma^2_{OW(CI)}$ is the uncertainty variance of the $B_{OW(CI)}$ estimations, and $\sigma^2_{OW(CI)_W}$ and $\sigma^2_{OW(CI)_I}$ are the estimated precisions of the $B_{OW(CI)}$ algorithms for 0% and 100% SIC, respectively. For the specific coefficients of Equa-

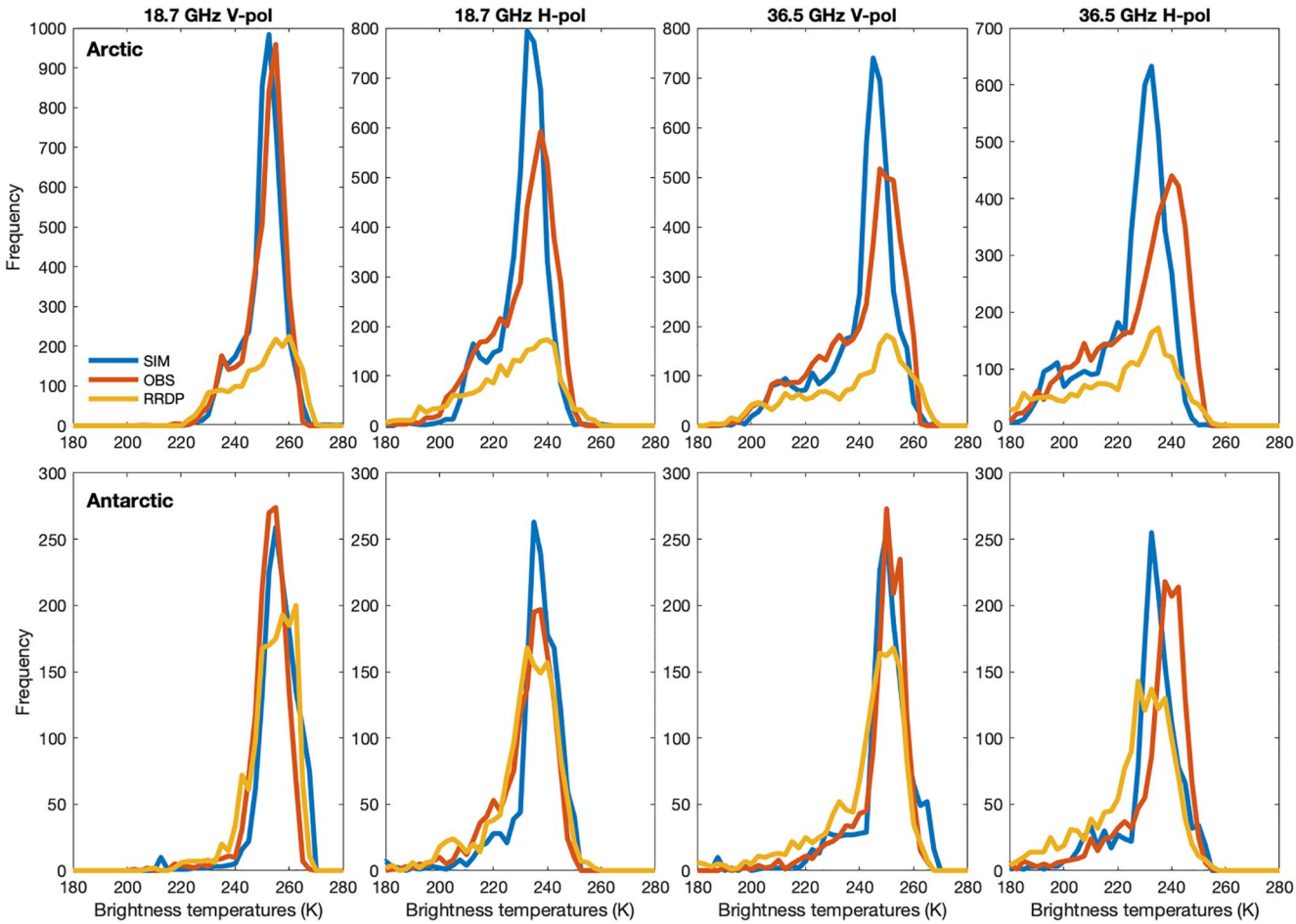

Figure 5. Histograms of the sea ice radiative transfer simulations at the Copernicus Imaging Microwave Radiometer vertically (V-pol) and horizontally (H-pol) polarized channels, at 18.7 GHz (left) and 36.5 GHz (right), for the Arctic (top, TBs from days 2016/12/17 and 2017/03/14) and Antarctic (bottom, 2017/06/15 and 2017/09/15). Plotted the simulated (SIM), observed (OBS, corresponding to Advanced Microwave Scanning Radiometer 2), and Round Robin Data Package brightness temperatures.

tions 4 and 5, the values 4.68% (σ_{OW_W}), 6.65% (σ_{OW_I}), 8.34% (σ_{CI_W}), and 4.09% (σ_{CI_I}) can be used to propagate the uncertainty to the final SIC estimate by using the same linear weighting as in Equation 6, but in terms of variances.

The hybrid algorithm exploits the TBs observed at Ku and Ka bands and therefore results in a SIC estimation at ~5 km, which is the resolution requested for the SIC. Using the lower C and X-bands can reduce uncertainties (Lavergne et al., 2019), but requires overcoming the problem of the coarser resolution of these channels. Algorithms working in this direction were recently published (Kilic et al., 2020; Prigent et al., 2020) and could be tested within the CIMR simulator in future performance evaluations.

3. Results

3.1. CIMR Simulated Observations

The forward radiative transfer model is fed with the geophysical fields and run at the initial 4 km resolution for each global scene, to produce global TB fields. This is followed by instrument geometry and antenna patterns calculations for a few selected orbits, resulting in the TAs that would be measured by CIMR for each antenna feed horn, frequency, and polarization.

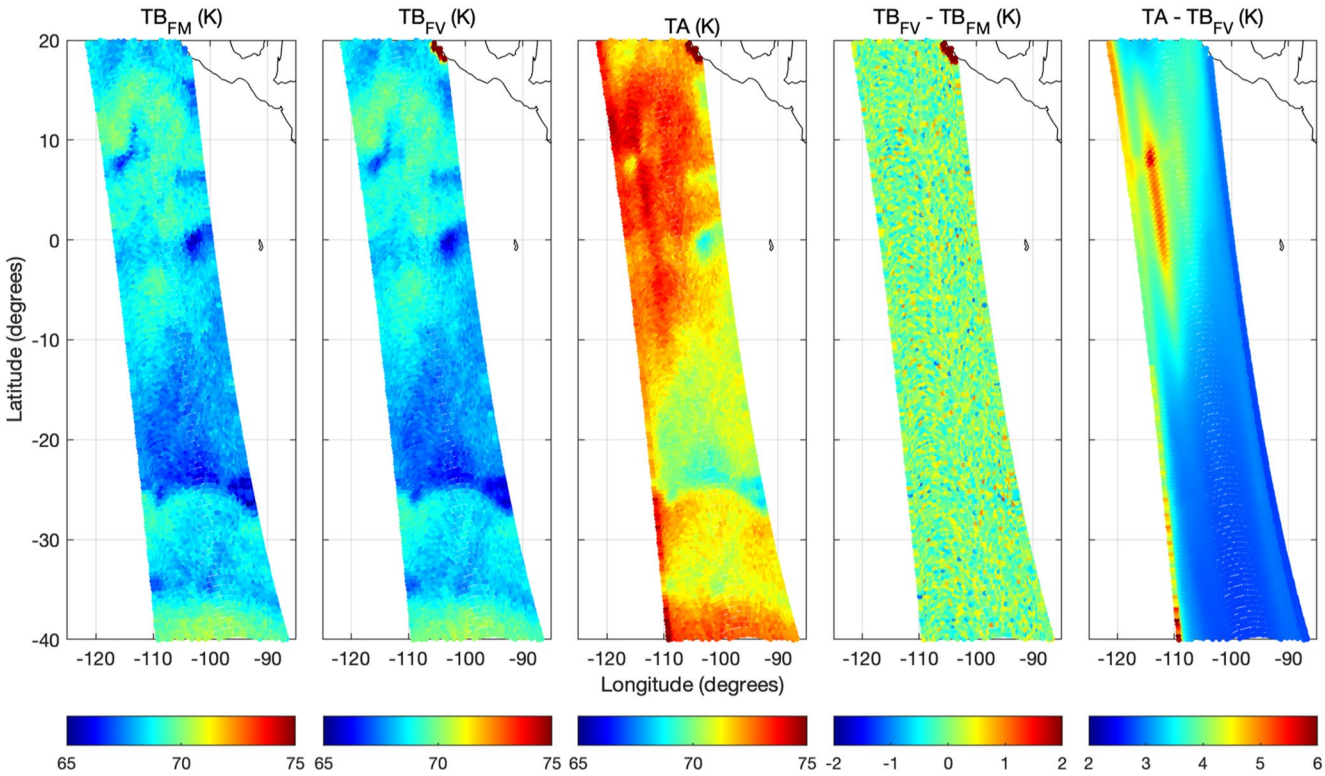

Figure 6. Simulated horizontally polarized 1.4 GHz brightness temperature (TB) for a Copernicus Imaging Microwave Radiometer orbit crossing the Atlantic Ocean the 2016/12/16. Plotted the top-of-atmosphere TBs as calculated by the forward model (TB_{FM}, no sensor), the convolution of the previous TBs with the antenna patterns at the locations of the radiometer fore views (TB_{FV}, but without modeling the Sun, Galactic, and ionospheric contributions), the antenna TBs (TA, with the previous contributions added), and the differences TB_{FV} - TB_{FM} and TA - TB_{FV}.

3.1.1. Open Ocean Forward Modeling

An example of the open ocean forward modeling is given in Figure 2. The forward model has been run with the geophysical fields of day 2017/09/15 at the 4 km gridding of these fields. The main variables affecting the radiative transfer are the SST, SSS, OWS, TCWV, and TCLW. Their fields (left) show the expected geographical patterns and gradients for this time of the year. The corresponding TB fields produced by the forward model simulator are displayed (middle, only showing the simulations for the vertically polarized channels). To evaluate them, their differences with SMAP and AMSR2 observed TBs interpolated to the same 4 km grid are also displayed (right). AMSR2 includes the CIMR channels at C, X, Ka, and Ku bands, and observes at a similar 55° incident angle. SMAP L-band radiometer has a real-aperture antenna like CIMR, and on-board hardware for detection and filtering of RFI technology to mitigate TBs contamination, which facilitates comparisons with modeled TBs as in Kilic et al. (2019). However, it observes at an incident angle of 40°. Therefore, the forward modeling at L-band has been prepared at 40° to make possible the forward modeling comparison with the SMAP observations here, and at 55° for the remaining CIMR simulations in the paper.

In most regions, the differences are quite small, indicating that the simulations and observations have comparable structures and gradients. The largest differences occur around some cloud systems associated with large liquid water values and strong surface winds, and for the higher frequencies, which are more sensitive to the atmospheric conditions. These discrepancies are related to both inaccuracies in the geophysical inputs (e.g., misplacement of the weather fronts) and the forward radiative transfer (e.g., errors in the sea surface emissivity for strong winds).

The statistics of the comparison are quantified in Figure 3. The biases are plotted before and after the bias correction implemented in the forward simulator (see Section 2.2.2). The biases before correction agree well with the values reported in Kilic et al. (2019) and are representative of the current status of the sea surface emissivity

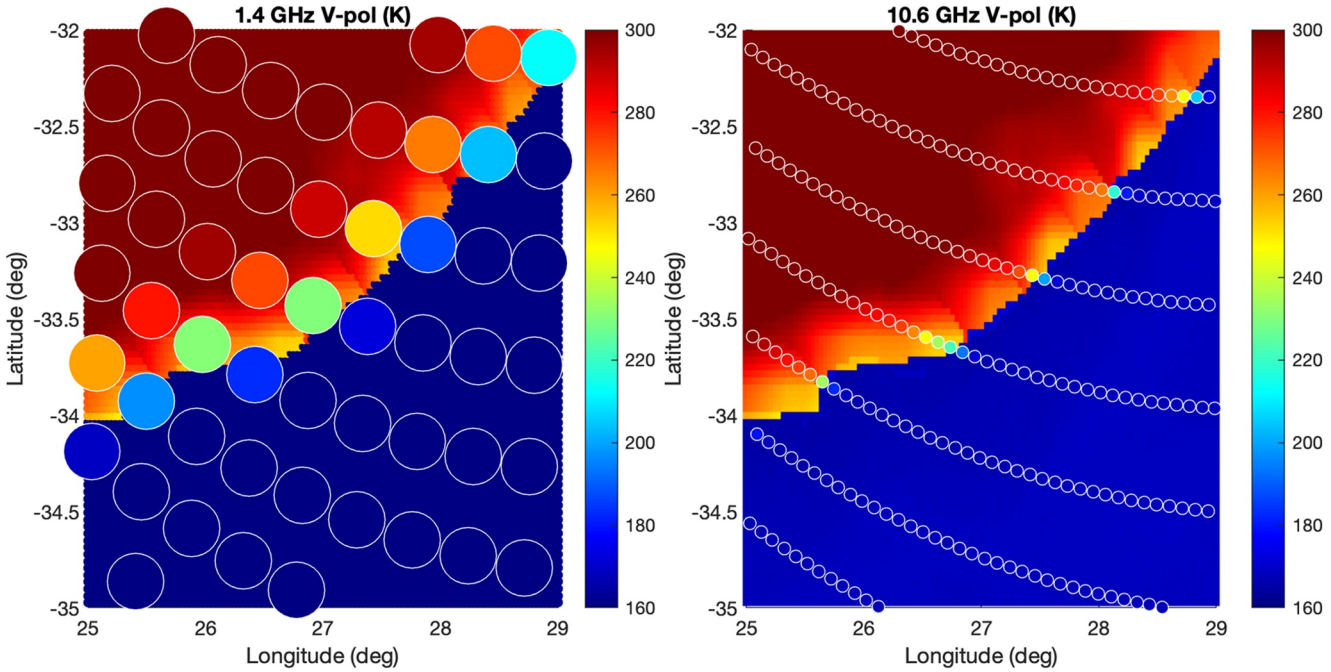

Figure 7. Simulated vertically polarized brightness temperatures (TBs) off the coast of South Africa on 2016/12/17. The background represents the 4 km initial top-of-atmosphere TB calculations. The colored dots show the location of the fore views for each 1.4 GHz (left) and 10.6 (right) GHz Copernicus Imaging Microwave Radiometer observations for one orbit (only displayed for one horn), with the colors indicating the resulting Antenna brightness Temperatures (TAs), after the antenna integration. Notice that the size of the colored dots displaying the TAs does not represent the true footprint size of the observations.

model adopted here for the open sea radiative transfer. As expected, debiasing the model using the results of the comparison between observed and modeled fields presented in Kilic et al. (2019) strongly reduces the biases. Overall, this comparison shows the realism of the forward model simulations over the open ocean and their ability to correctly reproduce the observations, for a large range of environments all over the globe, giving confidence, first in the description of the scene, and second, in the forward simulator.

3.1.2. Sea Ice Forward Modeling

Examples of Arctic and Antarctic sea ice forward simulations at 18.7 GHz are given in Figure 4 for two contrasting days (2017/03/14 and 2017/09/15). The implemented retrieval algorithm (Section 2.5) uses these two CIMR bands to derive the SIC estimates. For comparison with observed TBs, the AMSR2 measurements interpolated to the 4 km grid of the simulations are also plotted. The strong contrast between the open sea and sea ice TBs is visible. Strong gradients are also observed in the sea ice covered regions, related to the changes in ice conditions. The gradients are also observed in the AMSR2 fields, and although discrepancies between the simulated and observed TBs are noticeable, overall the simulated fields can be considered realistic.

The comparison between simulations and observations is further illustrated in Figure 5. Histograms of the simulated and observed winter TBs for both regions are presented. For the Arctic (Antarctic), the scenes of 2016/12/17 and 2017/03/14 (2017/09/15 and 2017/06/15) are selected. As described in Section 2.2.3, the sea ice emissivity has been parameterized using the observations contained in the RRDP, and histograms of the RRDP TBs for the same frequencies and regions are also presented. Given the complexity of the sea ice emission, the different sampling times of the sea ice conditions between the RRDP and the global scenes, and the likely inaccuracies in the ice inputs driving the RRDP-based ice parameterization and the parameterization itself, a perfect match between the histograms of simulated and observed TBs is not expected. The largest discrepancies are observed at the 36.5 GHz horizontally polarized TBs, where the peak of the AMSR2 TBs histogram is slightly shifted with respect to the simulated and RRDP ones. Nevertheless, there is an overall strong resemblance between the histograms for both frequencies, polarizations, and hemispheres, indicating that the sea ice forward modeling is

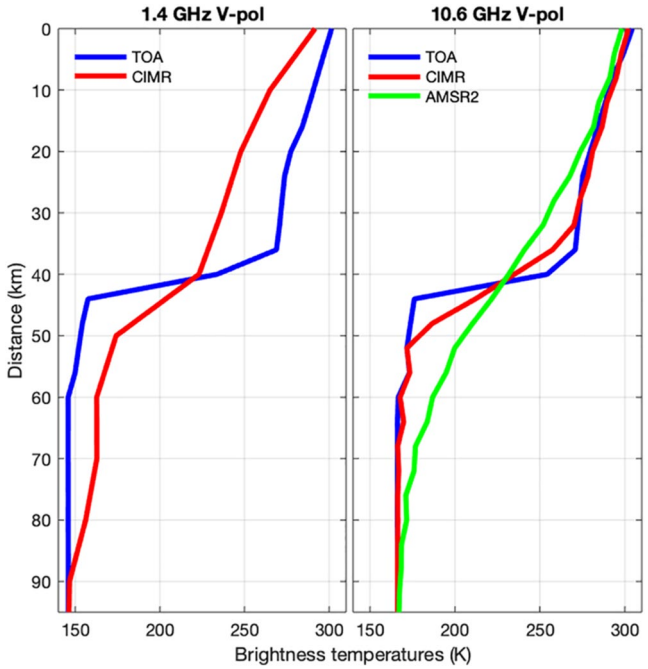

Figure 8. Zonal transect of the 1.4 (left) and 10.6 (right) GHz vertically polarized simulated brightness temperature (TB) in a 33.6°S to 35.1°S latitude band, averaged between 22°E and 24°E in longitude. Plotted the average for the 4 km initial top-of-atmosphere TBs and the Antenna brightness Temperatures (TAs) after the antenna pattern convolution (Copernicus Imaging Microwave Radiometer). For 10.6 GHz, the top-of-atmosphere TBs are also convolved with a simplified 3 dB antenna pattern to simulate TAs from an Advanced Microwave Scanning Radiometer 2-like sensor.

realistic enough to allow an evaluation of the CIMR performance for sea ice conditions even at large scales.

3.1.3. Sensor Modeling

The global TBs fields discussed in Sections 3.1.1 and 3.1.2 are convolved with the antenna patterns of each radiometer horn to reproduce the CIMR observed TAs. An example of this contribution at L-band from a CIMR simulation of an orbit crossing the Atlantic Ocean the 2016/12/16 is given in Figure 6. The first 2 plots show maps of the 1.4 GHz horizontally polarized top-of-atmosphere TBs as calculated by the forward model at the original 4 km resolution (TB_{FM}), and the convolution of the previous TBs with the antenna patterns at the locations of the radiometer fore views (TB_{FV}). For these two TBs the Sun and Galactic contributions, as well as the Faraday rotation and ionospheric interaction, have not been modeled for illustrative purposes. The third plot displays the antenna temperatures TA with the latter components added. The fourth plot shows the differences between TB_{FV} and TB_{FM}. These differences are due to the antenna integration and are most noticeable at places where there are strong TBs gradients. This can be the case in open sea regions if there are strong variations in SST or SSS, at the sea ice edges due to the larger differences between ice and sea emissivity, and close to the coastline due to the strong contrast in emissivity between land and sea. The latter case is visible in this example, with the largest differences close to the coastline of Central America. The last plot gives the differences between TA and TB_{FV}. The large values of the needle-like shape are mostly due to the Galactic glint, while the Sun glint is responsible for the large values at the left edge of the satellite track. Differences are relatively large at some places, such as the needle-like pattern caused by the Galactic glint, or the high values at the left edge of the satellite track caused by the Sun glint, showing the importance of properly modeling the L-band Sun and Galactic glitter for a realistic representation of the TA.

To further illustrate the impact of land contamination on ocean TBs, a zoom of the simulated TBs for an orbit crossing the coastal region south of Africa is presented in Figure 7. The 1.4 and 10.6 GHz vertically polarized TAs are plotted as colored dots centered at the horn positions of the fore views, while the colored background represents the original 4 km top-of-atmosphere TB fields. Notice that the size of the colored dots displaying the TAs does not represent the true footprint size of the observations and that only the positions of one horn are displayed to simplify the picture. At 10.6 GHz the CIMR instrument simulated here has 4 horns, but only the TAs of one horn is plotted. As expected, the effects of the antenna pattern at 1.4 GHz (spatial resolution of 60 km) are most noticeable in the coastal region where the strongest TA gradients are observed. Due to the much finer spatial resolution at 10.6 GHz, the impact of the convolution at this band is more limited.

To see the effect of the sensor modeling as a function of the distance to the coast, Figure 8 shows transects of vertically polarized TAs in a region (33.6°S–35.1°S, 22°E–24°E) from the same orbit crossing of the previous scene. They are built by averaging in the given longitude band the existing TAs and the original forward model TBs at 4 km resolution. For comparison purposes, a similar transect is built by simulating an AMSR2-like instrument based on a Gaussian averaging using as 3-db antenna pattern beamwidths the values given in Table 3. The advantage of the CIMR 10.6 GHz channel's finest spatial resolution is evident in order to reduce land contamination in the sea TAs.

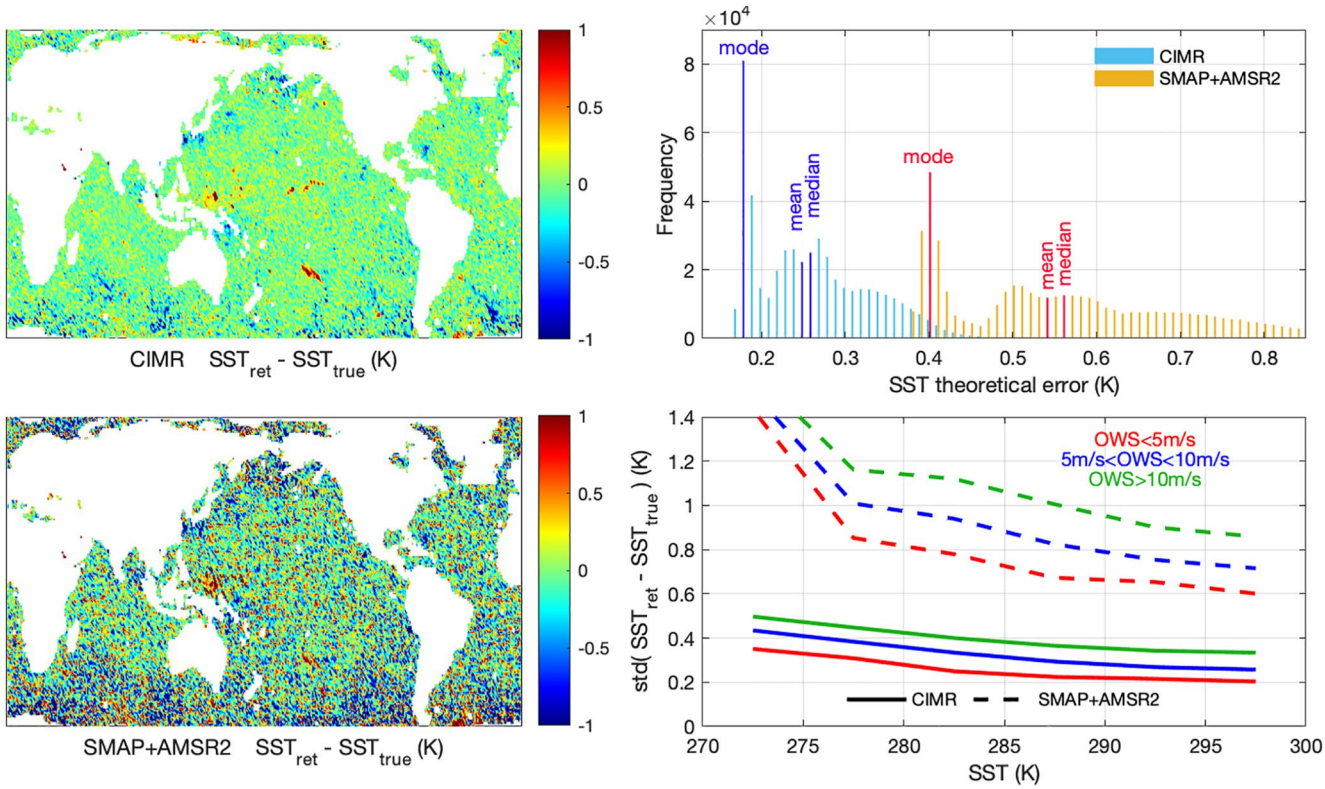

Figure 9. Summary of sea surface temperature (SST) retrieval performance from Copernicus Imaging Microwave Radiometer (CIMR) and an imaginary instrument simulated by adopting SMAP and AMSR2 main technical characteristics. Plotted the differences between the retrieved and true SST (SST_{true}) for the simulated scene of Figure 2 (top-left for CIMR, top-bottom for SMAP + AMSR2), histograms of the theoretical error associated with the retrievals (top-right), and standard deviation of the retrieved and true SST differences for several SST and ocean wind speed conditions (bottom-right).

3.2. CIMR Retrieved Products

3.2.1. Ocean Products: Global Scenes

The ocean inversion algorithm jointly retrieves SST and SSS using the algorithm described in Section 2.4. It is first tested on the 4 global scenes at the spatial resolution of the geophysical inputs for the scene (4 km) by inverting not the TAs, but the original forward model TBs with instrumental noise added. Inverting the TBs makes it possible to isolate the impact of the retrieval and instrument radiometric noises, from the effect of the instrument scanning geometry and spatial resolution. For each location, the simulated TBs are perturbed with instrument noise to simulate either CIMR, or the SMAP + AMSR2 combination, which are then inverted separately using the iterative retrieval algorithm procedure and corresponding x_a, S_a, and S_e, as described in Section 2.4.

A summary of the SST retrieval performance for both noise configurations is given in Figure 9. Maps of the difference between the retrieved and true SST for the 2017/01/15 simulations presented in Figure 2 are given in the left panels. As expected, the SMAP + AMSR2 configuration shows larger retrieval errors, related to its higher NEΔT values. For CIMR, the largest differences typically happen in areas of strong winds and large liquid water values. The distributions of the theoretical error given by Equation 3 are shown in the right-top panel, together with the distribution primary mode, mean, and median values. The 0.3 K requirement (see Table 1) is met by these simulations. Note also that the distribution shows secondary modes close to the mean value. These secondary modes are related to large wind speeds that induce larger SST errors, conditions that are sampled quite often in the four available global scenes. This is further illustrated in the bottom-right panel, where the standard deviation of the retrieved and true SST for different SST and OWS conditions is plotted. The difference increases from 0.15 K for warm waters and low winds to higher values up to 0.45 K for cold waters and high winds. The increase of the SST error with decreasing SST is physically related to the sensitivity of the signal to the SST due

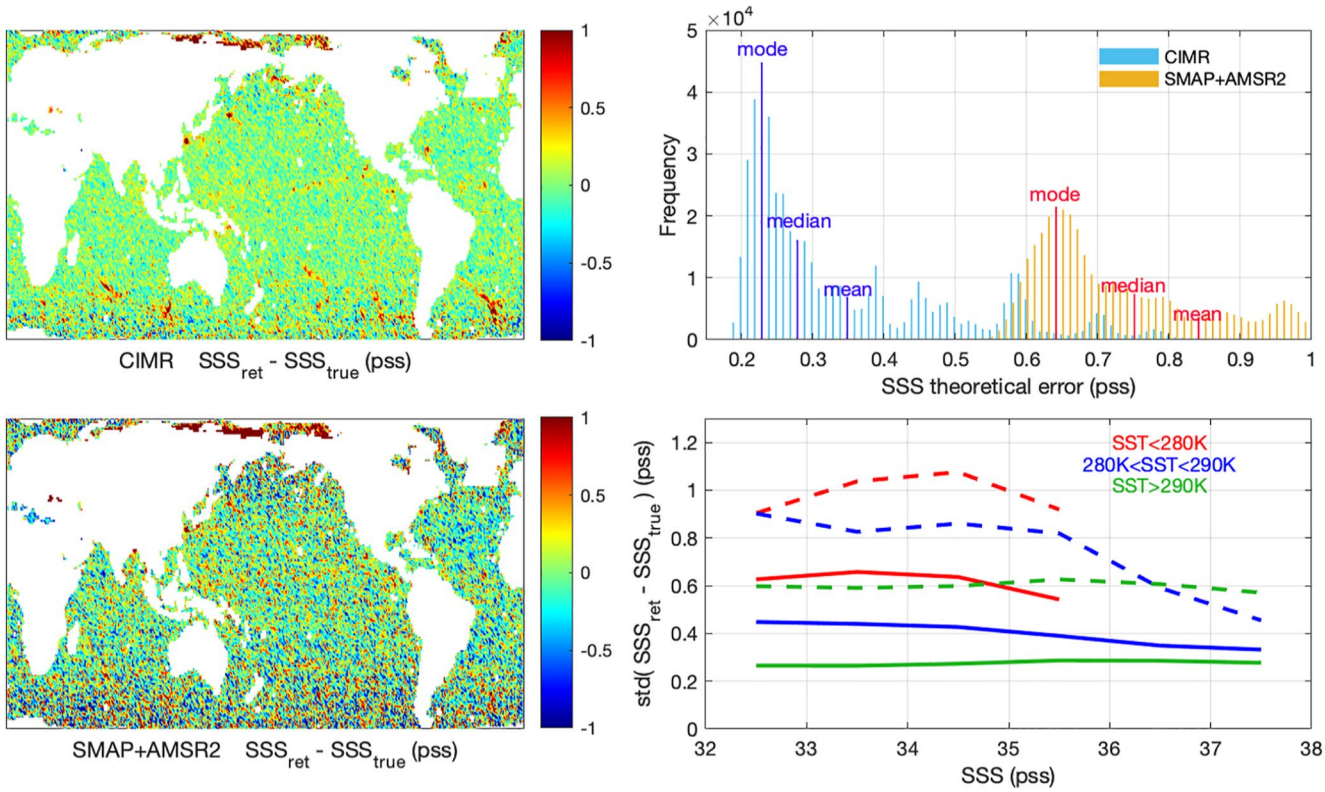

Figure 10. As Figure 9, but for the sea surface salinity retrievals.

to the SST dependence of the dielectric properties of sea water. The error increase with increasing OWS is also evident, but note that the high OWS often also occurs in the region of large TCLW, especially below 40°S and above 50°N, where the TB inversions are more challenging due to an increased atmospheric radiative contribution at the higher frequency channels.

Similar plots for the SSS retrieval are shown in Figure 10. The CIMR uncertainty requirement for SSS is given in Table 1 for monthly results, as the SSS products typically require spatial and temporal averages to reduce measuring uncertainties (e.g., Meissner et al., 2018). The errors displayed in Figure 10 correspond to instantaneous measurements and show the largest differences happening in places with large TCLW, as was the case for SST. This is possibly related to the larger errors in the joint SST retrievals accompanying the SSS estimation and its impact on the SSS retrieval accuracy. The standard deviation of the retrieved and true SSS differences shows the dependence on the SST: the sensitivity of the TBs to changes in SSS is greater in warmest waters, so the errors are smaller. Note that the instantaneous accuracy provided here is within the monthly requirement. Although some sources of retrieval uncertainty are still not accounted for in these retrievals, such as the dependence of the surface roughness on wind direction, these first results indicate that the low noise receiver at L-band, along with the simultaneous use of the higher frequency observations to improve the knowledge of the ocean emissivity and atmospheric emission, will contribute to reduce the SSS uncertainty, compared to the retrievals from current L-band instruments.

3.2.2. Ocean Products: Instrument Orbit

In a second test, the TAs from the simulation of one CIMR orbit over the Pacific Ocean on 2016/12/17 are inverted. The inversions are similar to the previous ones, but the use of TAs requires some processing of the true SST and SSS values before estimating the retrieval error. To associate to each retrieval a true SST and SSS value, the original fields are linearly interpolated to the center of the TAs ground projected fields of view. How representative this value is of the area covered by the field of view depends on the homogeneity of the field. Therefore, a

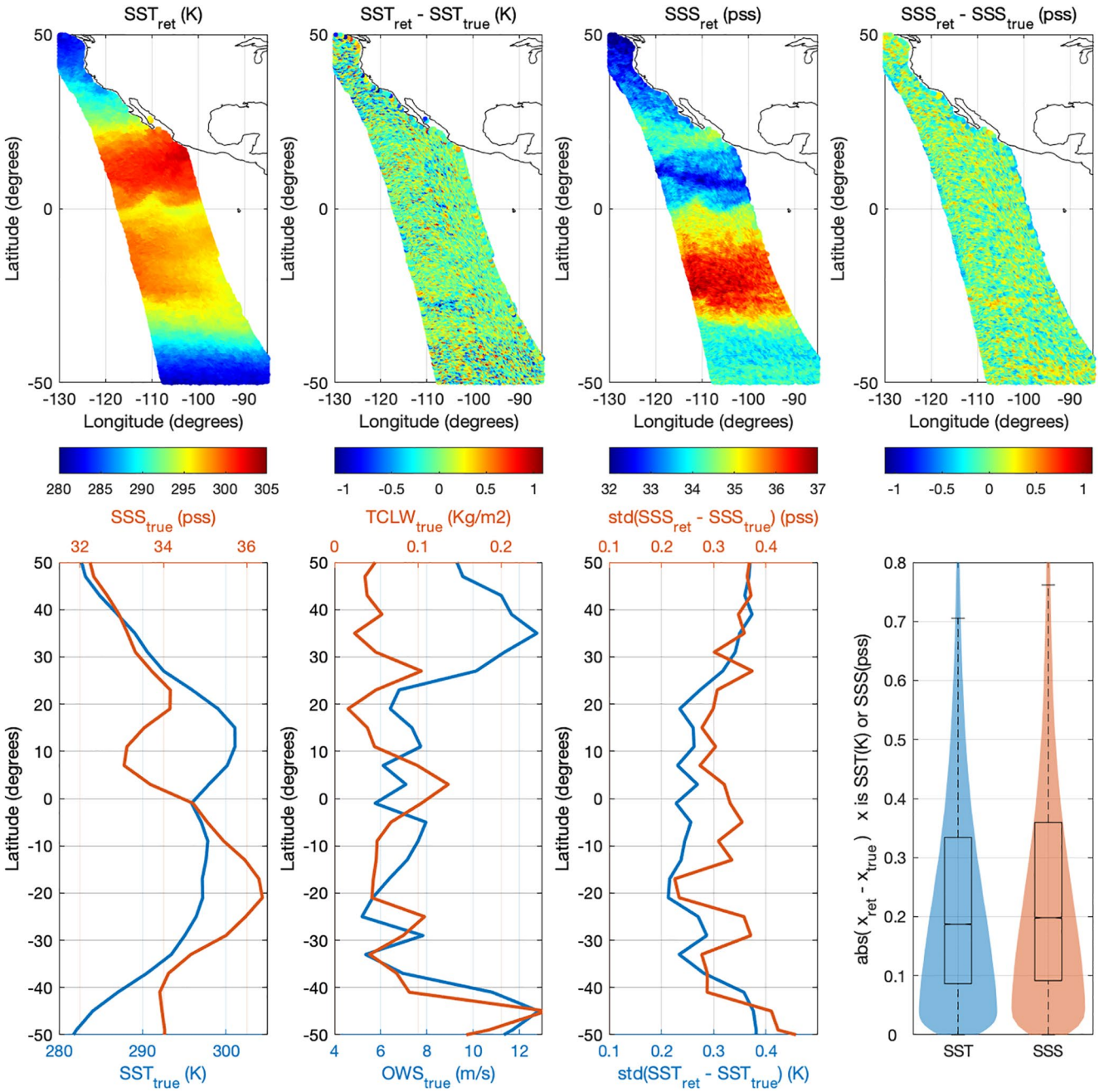

Figure 11. Summary of sea surface temperature (SST) and sea surface salinity (SSS) retrieval performance from an inversion of the TAs simulated for a section of a Copernicus Imaging Microwave Radiometer orbit crossing the Pacific Ocean on 2016/12/17. Plotted maps of the retrieved SST and SSS, and their difference with the SSS and SST true values (top), latitudinal transects of the true SST, SSS (bottom-first), ocean wind speed, total column liquid water (bottom-second), and the differences of the retrieved and true SST and SSS (bottom-third), and violin plots showing the distribution, median, and first and third quartiles of the absolute differences between retrieved and true SST and SSS (bottom-fourth).

one-to-one correspondence between geophysical fields and TAs does not exist any more, as is the case in the first inversion test with the original forward model TB fields.

The results of the TAs inversion are shown in Figure 11. The top panels show the retrieved SST and SSS, together with the differences between the retrieved and true values. The true values are, as discussed above, the true fields interpolated to the ground projected locations of the C-band fields of view. The bottom panels display latitudinal transects of the same true SST and SSS, together with the true OWS and TCLW fields prepared the

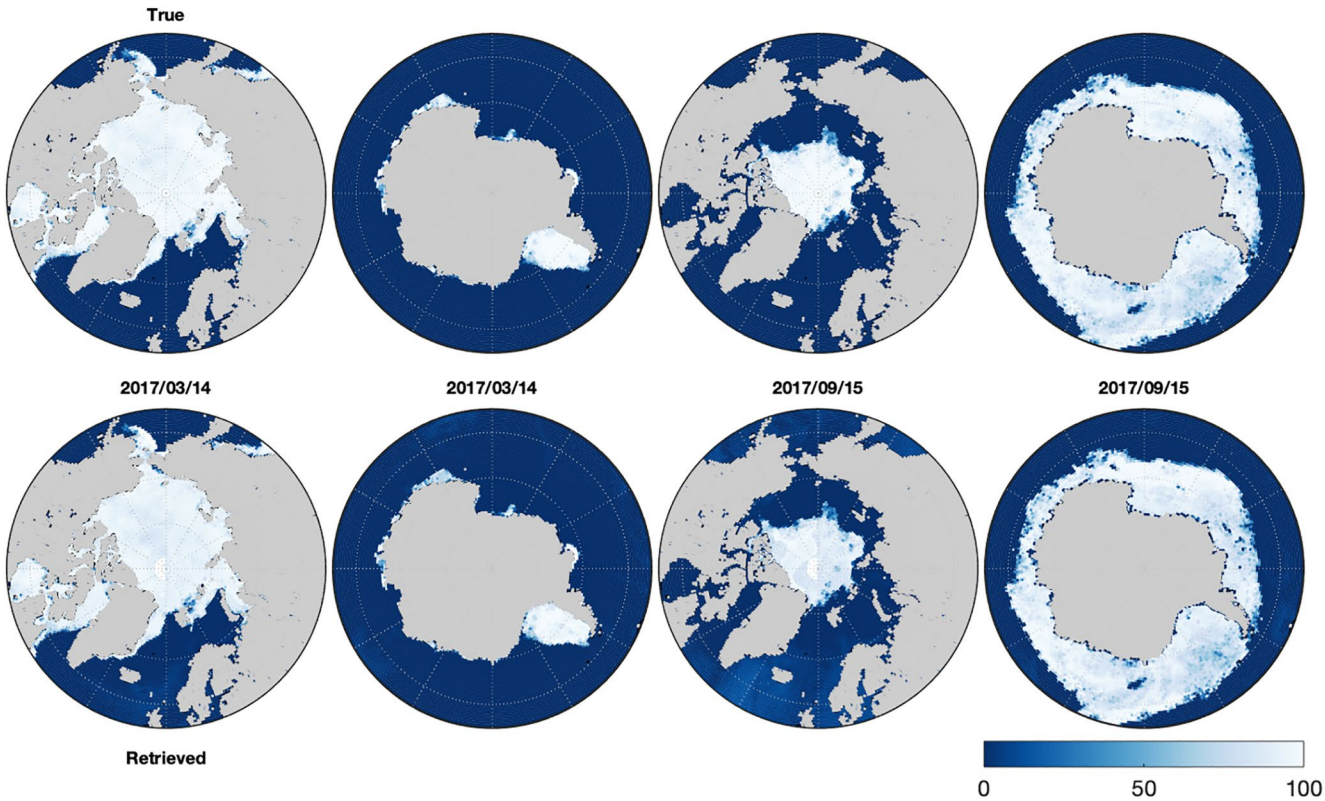

Figure 12. Maps of true (top) and retrieved (bottom) sea ice concentration in percentage for the days 2017/03/14 (left panels) and 2017/09/15 (right panels) for the Arctic and Antarctic.

same way. Transects of the retrieval error defined as the standard deviation of the retrieved and true SST and SSS differences are also given. For SST, the lowest error is close to 0.2 K coinciding with a region of low OWS and low TCLW. The increase in error at southern and northern latitudes associated with colder waters and larger OWS is evident. The SSS error curve also shows minimum values close to 0.2 pss in the same area, with a degradation of the error again toward the poles linked to the L-band smaller sensitivity to SSS and more uncertain SST estimation for cold waters. The final panel (bottom-right) shows violin plots giving the distribution of the retrieved SST and SSS absolute discrepancies with the true values, together with boxplots showing the median and first and third quartiles. For SST, the median value is below 0.2 K, indicating that for half of the retrievals the absolute discrepancies are below 0.2 K. For SSS, the distribution is similar, with also half of the absolute discrepancies below 0.2 pss.

3.2.3. Sea Ice Concentration: Polar Scenes

The performance of the SIC retrieval algorithm is first tested using the global scenes at the original forward modeling resolution. As for the ocean retrievals in Section 3.2.1, this allows comparing the retrieved SIC with a true SIC without any ambiguities related to the TBs antenna integration.

Figure 12 shows maps of the true and retrieved SIC values for the two global scenes having the minimum and maximum ice extensions in the Arctic and Antarctic. The ice extension is well replicated at both hemispheres and for both minimum and maximum extensions. To quantify the results, the Sea Ice Extent (SIE) defined by areas that have an ice concentration of at least 15% is calculated for the 4 global scenes and plotted separately for the Arctic and Antarctic in Figure 13. The relative errors, calculated as the difference between retrieved and true SIE and expressed as a percentage of the true SIE, are also shown. For these 4 situations, the relative errors are below 5% and confirm the good agreement shown by the SIC maps in Figure 12. Note that no tie-point adjustments are

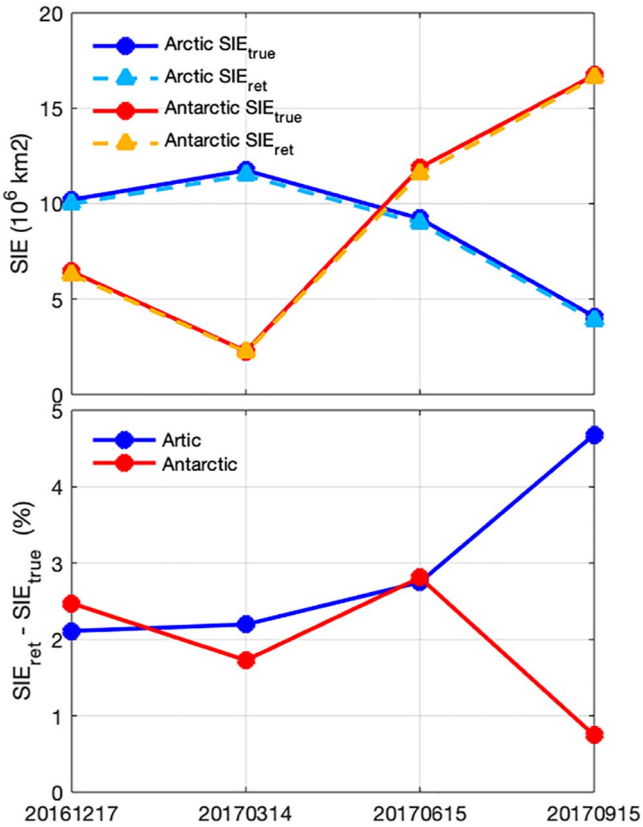

Figure 13. Arctic and Antarctic Sea Ice Extent (SIE) calculated from the retrieved and true sea ice concentration of the four global scenes. Plotted the SIE (top) and the difference between the retrieved and true SIE expressed as a percentage of the true SIE (bottom).

applied in the SIC algorithm, so this bias could possibly be further reduced with the dynamic tie-point formulation typically used in the operational algorithms (Lavergne et al., 2019).

Histograms of the retrieved SIC from the four global scenes corresponding to 0% and 100% true SIC are presented in Figure 14, separated for the Arctic and Antarctic regions. For comparison purposes, the SIC algorithm is also run on the TBs of the RRDP corresponding to the 0% and 100% SIC, and the resulting histograms are also shown. Only the winter months of the RRDP are considered for both poles, as the 100% SIC conditions in summer can be affected by melting conditions (Kern et al., 2020). Very close histograms for the CIMR and RRDP retrieval are not expected due to (a) the errors in the TB simulations over sea ice and ocean, as compared to real observations and (b) the different sea ice conditions sampled in the four global scenes and the available observations in the RRDP. Nevertheless, there is a significant agreement in the distribution modes and widths, which can be used as a confirmation of the realism of the simulated scenes. Comparing the Arctic and Antarctic distributions, the Antarctic SIC retrievals seem more biased than the Arctic ones. This is related to the specific coefficients used in Equations 4 and 5, more representative of the Arctic conditions. As discussed in Section 2.2.3, in operational applications, biases are suppressed by using region-dependent coefficients (Arctic and Antarctic) in dynamic tie-point formulations. Figure 14 also shows the retrieval errors estimated as the standard deviation of the retrieved SIC for both 0% and 100% SIC true values. Their values for the CIMR and RRDP retrievals differ but are comparable. In most cases, they are below the 5% standard uncertainty requirement, comparing well with the σ_{OW_W} and σ_{CI_I} uncertainty values presented in Section 2.5.

3.2.4. Sea Ice Concentration: Instrument Orbit

To illustrate the inversion of TAs, the retrievals corresponding to one orbit simulation over the Arctic and Antarctic on 2016/12/17 are shown in Figure 15. Maps of the retrieved SIC for the Arctic and Antarctic, and corresponding histograms of the retrieved SIC at 0% and 100%, are displayed. The retrieval biases are larger than in Figure 14. As these retrievals correspond to only one day, compared with the one day per season of Figure 14, the impact of not using the dynamic tie-point formulation is likely to be more visible. The standard deviations of the retrieved SIC are comparable to the previous retrievals. In these simulations, the impact of the instrument radiometric noise on the TBs is expected to be smaller than for the ocean retrievals as the SIC algorithm is very robust to small changes in TBs due to the strong contrast between ocean and sea ice emissivity. Regarding the spatial resolution of the simulated observations, only in areas with strong TB gradients, such as the marginal ice zone, the antenna convolution can have a significant impact. To study the SIC performance in those areas requires dedicated fine spatial resolution polar scenes where the effect of different pointing of the feeds and different fields of view can be properly simulated. This is currently in preparation within the CIMR simulator and will be addressed in further studies.

4. Conclusion

A first simplified end-to-end simulation of the CIMR mission has been presented. Although the final CIMR instrument design is still being finalized, the instrument baseline coming out of the mission Phase A/B1 is well defined, and a particular instrument implementation conforming to this baseline has been adopted in the study to show the expected CIMR performance. The simulation includes input parameters and processes such as test datasets, an instrument simulator, a forward model simulator, as well as the retrieval algorithms to derive the key ocean, sea ice, and atmospheric parameters.

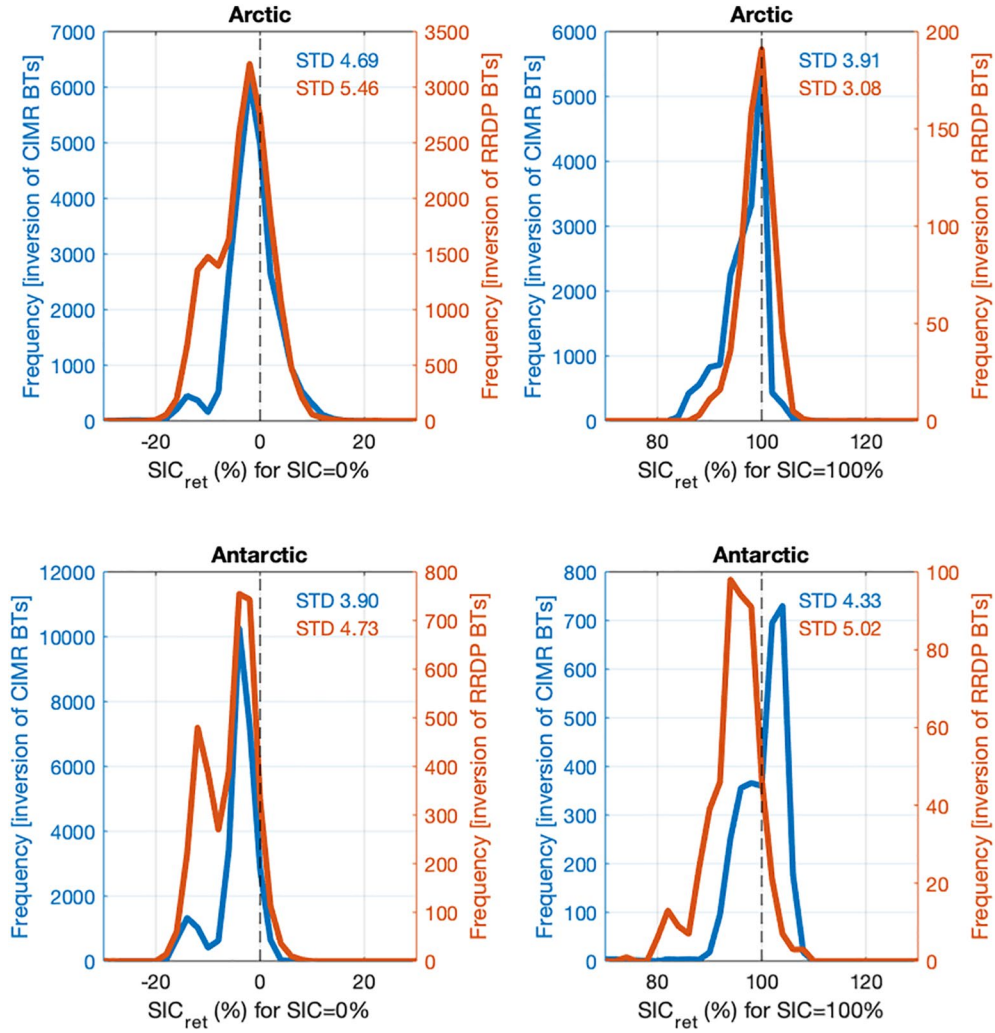

Figure 14. Histograms of the retrieved sea ice concentration (SIC) at 0% (left) and 100% true SIC (right) from the inversion of the simulated top-of-atmosphere brightness temperature (TBs) for the four global scenes. The retrievals are also run on the Round Robin Data Package (RRDP) TBs. The retrieval error estimated as the standard deviation of the retrieved SIC is indicated for the Copernicus Imaging Microwave Radiometer (blue) and RRDP (red) TBs.

Being a first simulation of the mission, the study concentrates on showing the realism of the simulated vertically and horizontally polarized TBs, together with an evaluation of the CIMR SST and SIC retrievals. Those variables are the two main mission objectives, and therefore their measurement requirements drive the instrument design. The third primary objective is to assure continuity of L-band and to illustrate the value of having the 1.4 GHz channel on board, simulations of the SSS measurement are also included.

The simulations are based on the forward modeling of four global scenes. Realistic input parameters to the forward model are sourced mainly from the ocean and atmospheric forecasts and reanalyses. For the open ocean and atmosphere forward modeling, off-the-shelf radiative transfer models are adopted. For sea ice, existing emission models are difficult to apply consistently at multiple frequencies at large scales, and an original and pragmatic emission parameterization based on observed data was implemented. The resulting top-of-atmosphere TBs over the open ocean and sea ice displayed realistic distributions. Comparisons to actual observations from the close-to-CIMR instrument (SMAP and AMSR2) showed good agreement and confirmed the realism of the simulations. This is of relevance in order to assure that the instrument simulation can be tested with inputs closely resembling the top-of-atmosphere TBs that would be observed by the real CIMR instrument.

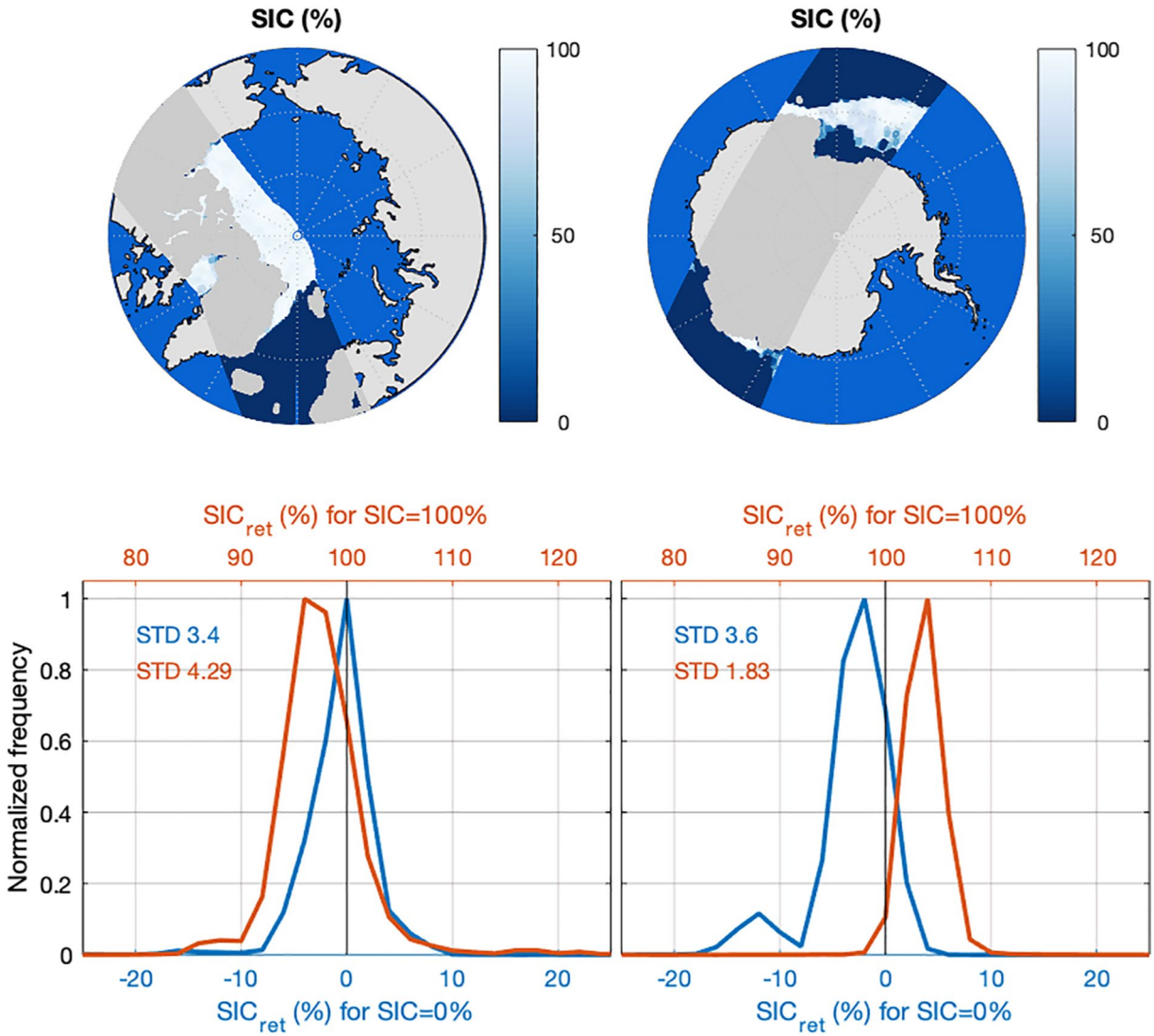

Figure 15. Summary of sea ice concentration (SIC) retrieval performance from an inversion of the Antenna brightness Temperatures simulated for a section of a Copernicus Imaging Microwave Radiometer orbit crossing the Arctic and Antarctic on 2016/12/17. Plotted maps of the retrieved SIC at the Arctic (top-left) and Antarctic (top-right), and corresponding histograms of the retrieved SIC at 0% and 100% (bottom). The retrieval error estimated as the standard deviation of the retrieved SIC has indicated for the 0% (blue) and 100% retrievals (red).

An orbit scenario and the generated top-of-atmosphere TBs are the main inputs for the instrument calculations simulating the time integrated antenna TAs. At L-band, the Sun and Galactic contributions, as well as the Faraday rotation, need to be accounted for. The generated TAs are then inverted by a retrieval algorithm based on an optimal estimation combining the multi-frequency observations of CIMR with the existing *a priori* knowledge of the variables to be retrieved. CIMR retrieval performance is then evaluated by comparing retrieved fields of SST, SSS, and SIC with the corresponding input fields to the simulation.

The evaluation of the retrieval performance showed that the technical characteristics of the simulated CIMR can provide SST, SSS, and SIC with precisions and spatial resolutions conforming with the mission requirements. The performance of a simplified imaginary instrument combining AMSR2 and SMAP main technical characteristics was also simulated to put CIMR performance in perspective. The evaluation also highlighted the challenges of observing the Arctic environment. The cold waters reduce the TB sensitivity to SST and SSS, which translates into larger retrieval errors. The retrievals are further impacted by the commonly occurring high winds and a larger atmospheric opacity associated with the typical presence of dense clouds. Regarding the SIC measurements,

the challenge is in areas of strong TB gradients, such as the marginal ice zone, where the impact of the different pointing of the feeds and different fields of view can be difficult to account for in the retrieval.

Future simulations need to be carried out during the next mission phases to include simulations of the third and fourth Stokes parameters, accommodate the updates to the instrument design, and test the impact of the evolution of the CIMR design in the retrieval performance. To fully exploit the low NEΔT of CIMR radiometers, work on further characterizing the forward modeling errors and how they propagate in the instrument simulations needs to be addressed. This gap has been identified by the Numerical Weather Prediction Community, and a reference quality model for ocean surface emissivity and backscatter from the microwave to the infrared (https://www.issibern.ch/teams/oceansurfemiss/) is currently under development and will be of benefit also for missions like CIMR. Regarding the test data sets, work on preparing local high resolution scenes to further investigate CIMR capabilities for highly heterogeneous surface conditions, such as close to the coastline, ice edges, or at places with strong SST or SSS gradients, has already started, and particular synthetic scenes to test specific instrument aspects will also be prepared and run through the simulator. Concerning the retrievals, addressing the CIMR performance for some of the other retrieval parameters, such as the ocean wind speed and direction, or the atmospheric column-integrated water vapor and liquid water, will be the subject of further analyses. CIMR provides a unique combination of frequencies. New retrievals that better exploit the full range of frequencies while benefiting from the higher spatial resolution will have to be tested in the new simulations (Kilic et al., 2020; Prigent et al., 2020).

With its large frequency coverage, improved spatial resolution, and radiometric precision, CIMR will provide the end user and the scientific community with key information on the fast changing Arctic environment. End-to-end simulations of the mission provide a critical tool to assess the expected capability of the CIMR instrument and will be continuously developed to gain further understanding of the CIMR performance in these challenging regions.

Data Availability Statement

All data used for this study are publicly available, and Copernicus services C3S and CMEMS, space agencies ESA, JAXA, and NASA, data centers ECMWF and NSIDC, the company RSS, and the University of Bremen, are acknowledged by contributing with their data to these simulations. The data can be accessed from the following repositories: C3S - https://cds.climate.copernicus.eu/cdsapp; CMEMS - ftp://my.cmems-du.eu/Core/GLOBAL_REANALYSIS_PHY_001_030/global-reanalysis-phy-001-030-daily; JAXA - https://gportal.jaxa.jp/gpr/; NASA - https://podaac-opendap.jpl.nasa.gov/opendap/allData/ghrsst/data/GDS2/L4/GLOB/JPL/MUR/v4.1/;NSIDC - https://nsidc.org/data/smap/smap-data.html; RSS - http://data.remss.com/ccmp/v02.0/; University of Bremen - https://seaice.uni-bremen.de/data/.

Acknowledgments
This work has been supported by the ESA CIMR-APE study (Contract number 400012555/18/NL/AI). We thank the CIMR Mission Advisory Group for productive discussions.

References

Bernard, R., Hallikainen, M., Kerr, Y., Kuenzi, K., Maetzler, C., Pampaloni, P., & Rast, M. (1990). *MIMR: Multifrequency passive microwave radiometer. Instrument panel report, ESA SP 1138*. ESA Publ. c/o ESTEC.

Burgard, C., Notz, D., Pedersen, L. T., & Tonboe, R. T. (2020). The Arctic Ocean Observation Operator for 6.9 GHz Part 2: Development and evaluation. *The Cryosphere*, *14*(7), 2387–2407. https://doi.org/10.5194/tc-14-2387-2020

Chaubell, J., Chan, S., Dunbar, R. S., Peng, J., & Yueh, S. (2019). *SMAP enhanced L1C radiometer half-orbit 9 km EASE-grid brightness temperatures, Version 2. Boulder, Colorado USA*. NASA National Snow and Ice Data Center Distributed Active Archive Center. https://doi.org/10.5067/XB8K63YM4U8O

Donlon, C. (2020). *Copernicus imaging microwave radiometer (CIMR) mission requirements Document*. version 4, ref. ESA-EOPSM-CIMR-MRD-3236. available from the European space Agency.

Duchossois, G., Strobl, P., Toumazou, V., Antunes, S., Bartsch, A., Diehl, T., & de Witte, E. (2018). *User requirements for a copernicus polar mission - phase 2 Report*. EUR 29144 EN (ISBN: 978-92-79-80960-6). https://doi.org/10.2760/44170

Duchossois, G., Strobl, P., Toumazou, V., Antunes, S., Bartsch, A., Diehl, T., & Nordbeck, O. (2018). *User requirements for a copernicus polar mission - phase 1 Report*. EUR 29144 EN (ISBN: 978-92-79-80961-3). https://doi.org/10.2760/22832

Hersbach, H., Bell, B., Berrisford, P., Hirahara, S., Horányi, A., noz Sabater, J. M., et al., (2020). The ERA5 global reanalysis. *Quarterly Journal of the Royal Meteorological Society*, *146*, 1999–2049. https://doi.org/10.1002/qj.3803

Kern, S., Lavergne, T., Notz, D., Pedersen, L. T., & Tonboe, R. (2020). Satellite passive microwave sea-ice concentration data set inter-comparison for Arctic summer conditions. *The Cryosphere*, *13*, 49–78. https://doi.org/10.5194/tc-14-2469-2020

Kerr, Y. H., Waldteufel, P., Wigneron, J. P., Martinuzzi, J., Font, J., & Berger, M. (2001). Soil moisture retrieval from space: The soil moisture and ocean salinity (SMOS) mission. *IEEE Transactions on Geoscience and Remote Sensing*, *39*, 1729–1735. https://doi.org/10.1109/36.942551

Kilic, L., Prigent, C., Aires, F., Boutin, J., Heygster, G., Tonboe, R. T., & Donlon, C. (2018). Expected performances of the Copernicus Imaging Microwave Radiometer (CIMR) for an all-weather and high spatial resolution estimation of ocean and sea ice parameters. *Journal of Geophysical Research: Oceans*, *123*(10), 7564–7580. https://doi.org/10.1029/2018jc014408

Kilic, L., Prigent, C., Aires, F., Heygster, G., Pellet, V., & Jimenez, C. (2020). Ice concentration retrieval from the analysis of microwaves: A new methodology designed for the Copernicus Imaging Microwave Radiometer. *Remote Sensing*, *12*, 1594. https://doi.org/10.3390/rs12071060

Kilic, L., Prigent, C., Boutin, J., Meissner, T., English, S., & Yueh, S. (2019). Comparisons of ocean radiative transfer models with SMAP and AMSR2 observations. *Journal of Geophysical Research: Oceans*, *124*(11), 7683–7699. https://doi.org/10.1029/2019jc015493

Kilic, L., Prigent, C., Jimenez, C., & Donlon, C. (2021). Technical note: A sensitivity analysis from 1 to 40GHz for observing the Arctic Ocean with the Copernicus Imaging Microwave Radiometer. *Ocean Science*, *17*(2), 455–461. https://doi.org/10.5194/os-17-455-2021

Lavergne, T., Sørensen, A. M., Kern, S., Tonboe, R., Notz, D., Aaboe, S., & Pedersen, L. T. (2019). Version 2 of the EUMETSAT OSI SAF and ESA CCI sea-ice concentration climate data records. *The Cryosphere*, *13*, 49–78. https://doi.org/10.5194/tc-13-49-2019

Maeda, T., Yugi, Y. T., & Imaoka, K. (2016). GCOM-W1 AMSR2 level 1R product: Dataset of brightness temperature modified using the antenna pattern matching technique. *IEEE Transactions on Geoscience and Remote Sensing*, *54*(2), 770–782. https://doi.org/10.1109/TGRS.2015.2465170

Marks, C., & Rodgers, C. D. (1993). A retrieval method for atmospheric composition from limb emission measurements. *Journal of Geophysical Research*, *98*, 14939–14953. https://doi.org/10.1029/93jd01195

Mathew, N., Heygster, G., & Melsheimer, C. (2009). Surface emissivity of the Arctic sea ice at AMSR-E frequencies. *IEEE Transactions on Geoscience and Remote Sensing*, *47*(12), 4115–4124. https://doi.org/10.1109/TGRS.2009.2023667

Meissner, T., & Wentz, F. J. (2012). The emissivity of the ocean surface between 6 and 90 GHz over a large range of wind speeds and earth incidence angles. *IEEE Transactions on Geoscience and Remote Sensing*, *50*(8), 3004–3026. https://doi.org/10.1109/tgrs.2011.2179662

Meissner, T., Wentz, F. J., & Le Vine, D. M. (2018). The salinity retrieval algorithms for the NASA Aquarius Version 5 and SMAP Version 3 releases. *Remote Sensing*, *10*, 1121. https://doi.org/10.3390/rs10071121

Meissner, T., Wentz, F. J., & Ricciardulli, L. (2014). The emission and scattering of L-band microwave radiation from rough ocean surfaces and wind speed measurements from the Aquarius sensor. *Journal of Geophysical Research: Oceans*, *119*(9), 6499–6522. https://doi.org/10.1002/2014jc009837

Nielsen-Englyst, P., Høyer, J. L., Alerskans, E., Pedersen, L. T., & Donlon, C. (2021). Impact of channel selection on SST retrievals from passive microwave observations. *Remote Sensing of Environment*, *254*, 112252. https://doi.org/10.1016/j.rse.2020.112252

Pedersen, L. T., Saldo, R., Ivanova, N., Kern, S., Heygster, G., & Tonboe, R. (2019). *Reference dataset for sea ice concentration (version 6)*. https://doi.org/10.6084/m9.figshare.6626549.v6

Prigent, C., Kilic, L., Aires, F., Pellet, V., & Jimenez, C. (2020). Ice concentration retrieval from the analysis of microwaves: Evaluation of a new methodology designed for the Copernicus Imaging Microwave Radiometer. *Remote Sensing*, *12*(7), 1594. https://doi.org/10.3390/rs12101594

Reul, N., Tenerelli, J., Chapron, B., & Waldteufel, P. (2007). Modeling sun glitter at L-band for sea surface salinity remote sensing with SMOS. *IEEE Transactions on Geoscience and Remote Sensing*, *45*(7), 2073–2087. https://doi.org/10.1109/tgrs.2006.890421

Reul, N., Tenerelli, J. E., Floury, N., & Chapron, B. (2008). Earth-viewing L-band radiometer sensing of sea surface scattered celestial sky radiation, Part II: Application to SMOS. *IEEE Transactions on Geoscience and Remote Sensing*, *46*(3), 675–688. https://doi.org/10.1109/tgrs.2007.914804

Rodgers, C. D. (1976). Retrieval of atmospheric temperature and composition from remote measurements of thermal radiation. *Reviews of Geophysics*, *14*(4), 609–624. https://doi.org/10.1029/rg014i004p00609

Rodgers, C. D. (2000). *Inverse Methods for Atmospheric Sounding: Theory and Practice* (Vol. 2). Series on Atmospheric, Oceanic, and Planetary Physics

Rosenkranz, P. W. (2017). *Line-by-line microwave radiative transfer (non-scattering)*. Code Library. https://doi.org/10.21982/M81013

Tenerelli, J. (2019). *CIMR algorithm development and performance evaluation (CIMR-APE): D-60, CIMR forward model Library*. European space Agency.

Tenerelli, J., Reul, N., Mouche, A. A., & Chapron, B. (2008). Earth-viewing L-band radiometer sensing of sea surface scattered celestial sky radiation, Part I: General characteristics. *IEEE Transactions on Geoscience and Remote Sensing*, *46*(3), 659–674. https://doi.org/10.1109/tgrs.2007.914803

Tonboe, R. T. (2010). The simulated sea ice thermal microwave emission at window and sounding frequencies. *Tellus, Series A: Dynamic Meteorology and Oceanography*, *62*(3), 333–344. https://doi.org/10.1111/j.1600-0870.2010.00434.x

Tonboe, R. T., Eastwood, S., Lavergne, T., Sørensen, A. M., Rathmann, N., Dybkjær, G., & Kern, S. (2016). The EUMETSAT sea ice concentration climate data record. *The Cryosphere*, *10*(5), 2275–2290. https://doi.org/10.5194/tc-10-2275-2016

UNESCO. (1985). *The international system of units (SI) in oceanography Tech. Rep. No. 32*. UNESCO Technical Papers No. 45.

Wang, D., Prigent, C., Kilic, L., Fox, S., Harlow, C., Jimenez, C., & Karbou, F. (2017). Surface emissivity at microwaves to millimeter waves over polar regions: Parameterization and evaluation with aircraft experiments. *Journal of Atmospheric and Oceanic Technology*, *34*(5), 1039–1059. https://doi.org/10.1175/jtech-d-16-0188.1